

Learning Optimization-inspired Image Propagation with Control Mechanisms and Architecture Augmentations for Low-level Vision

Risheng Liu, *Member, IEEE*, Zhu Liu, Pan Mu, Zhouchen Lin, *Fellow, IEEE*, Xin Fan, *Member, IEEE*, and Zhongxuan Luo

Abstract—In recent years, building deep learning models from optimization perspectives has become a promising direction for solving low-level vision problems. The main idea of most existing approaches is to straightforwardly combine numerical iterations with manually designed network architectures to generate image propagations for specific kinds of optimization models. However, these heuristic learning models often lack mechanisms to control the propagation and rely on architecture engineering heavily. To mitigate the above issues, this paper proposes a unified optimization-inspired deep image propagation framework to aggregate Generative, Discriminative and Corrective (GDC for short) principles for a variety of low-level vision tasks. Specifically, we first formulate low-level vision tasks using a generic optimization objective and construct our fundamental propagative modules from three different viewpoints, i.e., the solution could be obtained/learned 1) in generative manner; 2) based on discriminative metric; and 3) with domain knowledge correction. By designing control mechanisms to guide image propagations, we then obtain convergence guarantees of GDC for both fully- and partially-defined optimization formulations. Furthermore, we introduce two architecture augmentation strategies (i.e., normalization and automatic search) to respectively enhance the propagation stability and task/data-adaption ability. Extensive experiments on different low-level vision applications demonstrate the effectiveness and flexibility of GDC.

Index Terms—Low-level vision, image propagation, generative discriminative and corrective modules, propagative control mechanisms, architecture augmentation strategies



1 INTRODUCTION

RECENT decades have witnessed dramatic advancements in low-level vision applications, ranging from image restoration and enhancement [1], [2], [3], [4], [5], scene estimation [6], [7], [8], [9] and medical imaging [10], [11], just to name a few, based on numerical optimization [12], [13], [14], deep learning [4], [15], [16] and optimization-inspired learning methodologies [17], [18], [19]. Among them, optimization-inspired learning leverages the hybrid combination of task-oriented domain knowledge and data-driven principles directly, achieving the significant advancements for low-level vision.

However, the effective design to generate and control

proper image propagation¹ still remains as a challenging task.

In literature, classic optimization methods for addressing image-based tasks have been widely explored. Partial Differential Equations (PDEs) [12], [13] are one kind of representative methods to characterize the physical natures as mathematical understanding for low-level vision. Sparse priors (e.g., Total Variation (TV) prior [14], ℓ_0 prior [20] and hyper-Laplacian prior [21]) and heuristic priors (e.g., dark channel prior [22], extreme channel prior [23]) are introduced to regularize latent solution spaces for these optimization models (e.g., Maximum a Posteriori (MAP)-type models), due to the irreversibility of generating latent solutions. Utilizing classic numerical optimization schemes, such as Forward-Backward Splitting (FBS) [24], Proximal Gradient (PG) [25] and Alternating Direction Method of Multipliers (ADMM) [26], these optimization models can generate iterative energy minimization to obtain latent solutions. However, these methods are fully dependent on hand-crafted computation-complex priors, which cannot regularize real-world distribution completely and undermine the procedure of generating visual-pleasant or precise solutions.

During the past few years, a large amount of CNN-based learning methods have been proposed to learn generalizable and implicit models for particular tasks (e.g., degradation) from large-scale datasets. Among them, shallow

- Risheng Liu is with DUT-RU International School of Information Science & Engineering and the Key Laboratory for Ubiquitous Network and Service Software of Liaoning Province, Dalian University of Technology, Dalian 116024, China. He is also with the Peng Cheng Laboratory, Shenzhen, China. (Corresponding author, e-mail: rslu@dlut.edu.cn).
- Zhu Liu, Xin Fan and Zhongxuan Luo are with DUT-RU International School of Information Science & Engineering and the Key Laboratory for Ubiquitous Network and Service Software of Liaoning Province, Dalian University of Technology, Dalian 116024, China. (email: liuzhu_dlut@mail.dlut.edu.cn, xin.fan@dlut.edu.cn and zxluo@dlut.edu.cn).
- Pan Mu is with the School of Mathematical Sciences, Dalian University of Technology and also with the Key Laboratory for Ubiquitous Network and Service Software of Liaoning Province, Dalian, 116024, China. (email: mujifan11@mail.dlut.edu.cn).
- Zhouchen Lin is with the Key Laboratory of Machine Perception (Ministry of Education), School of Electronics Engineering and Computer Science, Peking University, Beijing 100871, China. (email: zlin@pku.edu.cn).

Manuscript received April 19, 2005; revised August 26, 2015.

¹ In this paper, we just refer to the forward propagations generated by numerical iterations and deep neural networks on images as “image propagation”.

CNNs [4], [15] have been firstly proposed, across chained propagative inferences in the feature domain. With effective building principles introduced to design training strategies and architectures such as residual learning [27], adversarial learning [28], encoder-decoders [29], dense blocks [6] and multi-scale inference [15], these CNN-based schemes obtain higher performances. However, these learning-based schemes are fully dependent on concrete CNN architectures and discard physical rules, limiting the flexibility of adopting into other tasks.

In recent years, optimization-inspired learning methods combine the learning-based priors (e.g., learnable filters [30], [31] and data-driven CNNs [32], [33]) and numerical schemes-based iterations, leveraging unrolling-based techniques. For instance, some studies in [30], [31] combine unrolled half-quadratic model with a set of high-order parametric filters as implicit priors for denoising and deblurring. Lately, a series of CNN-based modules [32], [33], [34] are embedded into the iteration-type frameworks to construct generative priors of energy models. Lately, a series of works [17], [18], [19] attempt to introduce the joint training strategies to improve performances by converting the fidelity and/or regularization into principled CNNs. These optimization-inspired methods show the promising results but their propagation behaviors cannot be guaranteed without suitable control mechanisms. Furthermore, the delicate architecture design and engineering experiences are essential to construct these hybrid learning methods.

To partially overcome the above issues, we propose a unified optimization-inspired framework to build deep image propagations for different low-level vision tasks. In particular, based upon “optimization learning” perspective, we first introduce three categories of principles to build our candidate (learnable) optimization modules. That is, we would like to propagate latent images (a.k.a., obtain the optimal solution) in Generative manner, based on Discriminative metric and with domain knowledge Correction (GDC for short). Both greedy and joint strategies can be utilized to train the corresponding GDC-based image propagation. By designing control mechanisms to guide the propagations toward our desired solutions, the convergence properties of GDC can be proved for both fully- and partially-defined optimization models. Furthermore, two architecture augmentation strategies (i.e, normalization and automatic search) are proposed to stabilize the image propagation and search more efficient architectures for GDC, respectively. Finally, we conduct experiments to analyze the behaviors and verify the efficiency of our propagative modules, control mechanisms and augmentation strategies. Comprehensive experimental results demonstrate that our GDC series methods achieve state-of-the-art performances on a variety of low-level vision tasks. In summary, our contributions are threefolds:

- Different from most existing approaches, which just build their image propagations by straightforwardly combining numerical iterations and manually designed architectures, GDC aggregates the generative, discriminative and corrective principles and provides a unified optimization perspective to construct our fundamental propagative modules.
- Our propagative control mechanisms can successfully guarantee the convergence properties of GDC for both fully- and partially-defined optimization models, thus is more flexible to guide image propagations for diverse low-level vision tasks (may have different kinds of formulations).
- We also introduce strategies to augment our propagative architectures (i.e., normalize architectures to enhance the propagation stability and automatically discover task/data-specific architectures from compact search space), thus our GDC is more suitable to address problems in complex real-world scenarios.

2 RELATED WORKS

2.1 Classical Optimization Methods

Classical optimization methods often formulate the physical rules as particular kinds of energy models. Thus by optimizing the obtained models with different numerical schemes [24], [25], [26], these methods can generate optimization iterations towards to desired solutions. One prominent category of these iterative methods is the MAP-type schemes. Owing to the ill-posedness of most image-based tasks, MAP-type schemes have introduced explicit sparse priors to construct the certain optimization formulations for regularizing the structures of latent solutions and characterizing the task-oriented knowledge. More specifically, TV prior [14] is robust for natural noise but is unable to preserve the image’s edges and textures well. The sparse ℓ_0 prior, which is non-convex and discontinuous, becomes the extensive regularizer to address various image-based tasks, such as text image deblurring [20] and smoothing [35]. Some ingenious priors such as dark channel prior [22], patch prior [36] and extreme channel prior [23] are also introduced to regularize the latent solutions space. These carefully designed priors provide the mathematical principles for regularizing the propagations. Nevertheless, with the complexity of real-world image-based tasks, it brings difficulties to introduce priors that regularize the latent distribution space and characterize the generative formations completely. These limitations make the purely prior-regularized propagations difficult to obtain solutions efficiently and accurately.

2.2 CNN-based Learning Methods

CNN-based methods have achieved considerable advancements on various image-based tasks. These methods generate the heuristic data-driven mapping from observations to desired solutions straightforwardly. Numerous CNN architectures based on different principles are applied to build task-specific schemes to solve dedicated type of degradation respectively. For non-blind deconvolution, the method proposed in [4] tries to establish separable structure of network based on the optimization-based principles. Based on different principles (e.g., multi-scales models [29] and generalized low-rank approximation [37]), diverse types of CNNs are introduced to obtain promising results. On the other hand, for blind deblurring, a multi-scale CNN [15] is developed to solve dynamic blurred scenes. Nevertheless, this methods can not handle with arbitrary size of motion

blur kernels. As for image deraining, a principled shallow CNN [38] is proposed firstly to infer rain streaks and clear backgrounds. Context aggregation principle [39], non-local encoder-decoder [40] and progressive residual blocks [41] are introduced to establish more complex architectures with higher performances. Neural Architecture Search (NAS) method [42], [43] proposed innovative paradigms to obtain task-specific architecture for high-level vision. Lately, a few recent studies [27], [44] attempt to construct universal frameworks to address the multiply degradation scenarios by investigating the similarities of degradation from related tasks. However it is indeed difficult and considerable time needed to collect or generate sufficient real-world clear/degraded training pairs. However, without the explicit guidance and enforcement of physical rules, these solutions are sensitive to challenging low-level applications.

2.3 Optimization-inspired Learning Methods

By unrolling the iterations of numerical optimization objectives, some methods attempt to utilize diverse principled modules as priors to plug into iterations and combine optimization-inspired learning schemes. One typical learning-based optimizations based on unrolling techniques, combining the parametric priors and iteration-based models, aiming to model the relationship between observations and clear images. For instance, the Cascade of Shrinkage Fields (CSF) [30], [31] learn a series of filters as discriminative regulations to construct hybrid frameworks, leveraging the additive form of Half-Quadratic Splitting (HQS) and learnable shrinkage fields. On the other hand, in [45], the classical Trainable Non-linear Reaction Diffusion (TNRD) scheme is also developed by training the unrolled gradient descent inference steps jointly. ADMM-Net [46] combines the hyperparameters learning and deep architectures, unrolling the iterations of ADMM schemes to build a unified and trainable optimization scheme for MRI reconstruction. Recent studies introduce many plug-in schemes by unrolling-based techniques to deal with fidelity term and prior term respectively for generate the hybrid propagations. In [47], this method introduce the implicit denoiser modules as regularization to plug into numerical iterations. Very lately, pre-trained CNN-based modules [32], [33] are implemented to solve many image restoration tasks such as image denoising, deconvolution and super-resolution, based on optimization unrolling. However these methods may lack of mechanisms to control iterative behaviors to avoid local minimum.

Moreover, there are also some recent studies develop the hybrid CNN-based methods for jointly training such as Dr-Net [18] and plugged autoencoders [17] to model the fidelity and/or prior of energy models to enhance performances. Furthermore, CNN-CRF [19] combines two kinds of architectures (i.e., CNN and CRF) in straightforward manner to build the network for semantic segmentation, but lacks control mechanisms and relies on manually designed architectures. In contrast, our GDC constructs three principled modules from a unified optimization perspective and introduce two propagative control mechanisms to obtain theoretical guarantees for the propagation. Architecture augmentation strategies also can provide the stable propagation and design task-specific architectures. These proposed techniques

actually can help us obtain more powerful GDC and are all significantly different from the CNN-CRF method.

3 THE PROPOSED GDC IMAGE PROPAGATION

As aforementioned, most low-level vision problems can be (partially) formulated as energy-based optimization models. Based upon “optimization learning” perspective, we first define the following generic composite optimization formulation

$$\min_{\mathbf{u}} \Psi(\mathbf{u}) := f(\mathbf{u}) + \phi(\mathbf{u}), \quad (1)$$

where \mathbf{u} is denoted as one sought signal or image for our considered low-level vision task, f is data fidelity function for capturing the physical rules (e.g., the degradation formations) and ϕ denotes the prior term, related to the approximation of latent distributions of solutions.

Specifically, we can classify existing energy-based models into two categories of optimizations, fully- and partially-defined models. Fully-Defined Model (FDM, for short) has clear handcrafted prior and task-oriented fidelity, deriving from Eq. (1). In contrast, Partially-Defined Model (PDM, for short) does not have concrete prior formulations, which exploits learnable data-driven regularization terms from paired training sets to optimize Eq. (1) implicitly.

The main goal of this paper is to aggregate different categories of principles to propagate images towards task-specific solutions, aiming to deal with the weaknesses of prior dependency of numerical schemes, domain knowledge ignorance of CNN-based learning and control mechanisms lack and architecture limitations of optimization-inspired learning.

3.1 Propagative Modules

In this subsection, we propose three fundamental modules to propagate images towards to the task-specific solution of Eq. (1) by utilizing generative, discriminative learning principles and domain knowledge correction respectively.

Generative Module: Considering to predict optimal task-specific solutions from objective Eq. (1) straightforwardly, we establish Generative Module (i.e., GM) within the propagation framework. Indeed, the direct scheme to obtain task-specific solution is to introduce a conceptual descent scheme to propagate \mathbf{u} towards to the optimal solution, i.e., $\mathbf{u}^{t+1} \leftarrow \mathbf{u}^t - \frac{\partial \Psi(\mathbf{u}^t)}{\partial \mathbf{u}^t}$, assuming the objective as a whole formulation, where $\frac{\partial \Psi(\mathbf{u}^t)}{\partial \mathbf{u}^t}$ denotes the (sub)-gradient of Ψ at \mathbf{u}^t . Notice that, in order to simplify this formulation, we ignore the learning rate.

Consequently, instead of adopting numerical-based gradient calculations, we introduce a CNN architecture $\mathcal{G}(\mathbf{u}^t; \omega_g)$ (i.e., GM) to parameterize the descent direction $-\frac{\partial \Psi(\mathbf{u}^t)}{\partial \mathbf{u}^t}$ by investigating image statistics from training data. The concrete parameterized process of the above gradient updating scheme can be written as

$$\mathbf{u}_g^{t+1} \leftarrow \mathbf{u}^t + \mathcal{G}(\mathbf{u}^t; \omega_g), \quad (2)$$

where $\mathcal{G}(\mathbf{u}^t; \omega_g) := -\frac{\partial \Psi(\mathbf{u}^t)}{\partial \mathbf{u}^t}$ and ω_g denotes the learnable parameters. Focusing on different low-level vision tasks, we design task-oriented generative architectures by utilizing diverse construction strategies.

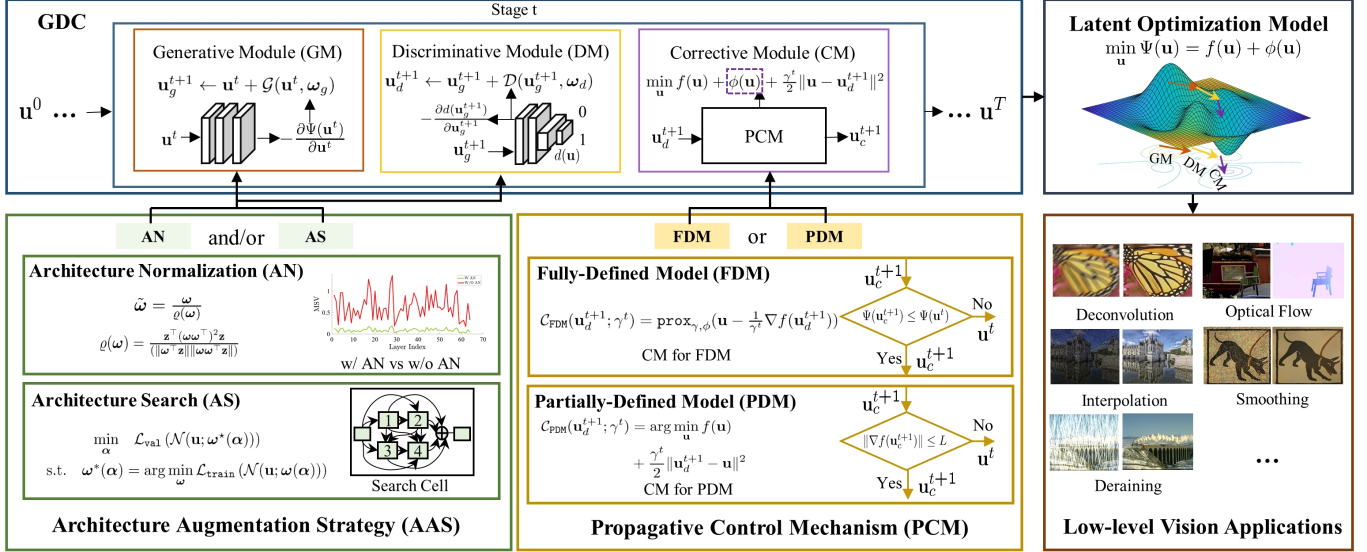


Fig. 1. Overview of the main workflow and components of GDC. We first illustrate the image propagation of GDC and the corresponding learning-based optimization trajectory on the top row. We then demonstrate the architecture augmentation strategies, the propagative control mechanisms and our considered low-level vision applications on the bottom row.

Discriminative Module: We then design our propagative module based on the discriminative learning principle, which is called Discriminative Module (i.e., DM). That is, we leverage the following sub-problem to formulate our discriminative propagation.²

$$\min_{\mathbf{u}} \|\mathbf{u} - \mathbf{u}_g^{t+1}\|^2 + d(\mathbf{u}), \quad (3)$$

where we consider $d(\mathbf{u})$ as a regularization function and it should provide lower responses for desired solutions and higher responses for observations. Different from conventional optimization-based methods, which design such regularization term based on explicitly formulated priors (e.g., ℓ_1 and TV), we parameterize $d(\mathbf{u})$ by a binary classification-based CNN, which can predict the task observation as positive (labeled as 1) and desired task-specific solution as negative (labeled as 0). In this way, we can write our Discriminative Module (DM) by performing gradient-based updating on Eq. (3), i.e.,

$$\mathbf{u}_d^{t+1} \leftarrow \mathbf{u}_g^{t+1} + \mathcal{D}(\mathbf{u}_g^{t+1}; \omega_d), \quad (4)$$

where $\mathcal{D}(\mathbf{u}_g^{t+1}; \omega_d) := -\frac{\partial d(\mathbf{u}_g^{t+1})}{\partial \mathbf{u}_g^{t+1}}$ and the metric of discriminative gradients can distinguish whether the solution is a task-specific solution or not. Similarly, we also ignore the learning rate in this formulation.

Note that though the similarly named modules are used in our framework and GAN, the learning methodologies of these modules are totally different. First, Discriminator in GAN can only be used to assist the training of Generator and we actually only use the trained Generator to propagate images for testing. In contrast, in GDC, our DM is designed as a single module and can independently propagate image using discrimination responses (between observations and desired solutions). Second, in GAN, the parameters of Discriminator cannot be updated individually, while we

can perform both greedy and joint training strategies to learn the parameters of our DM. In summary, GAN actually introduces Discriminator to perform the adversarial learning. On the contrary, DM can be used to generate forward propagation for any given learning models.

Corrective Module: Aiming to infuse the task-oriented domain knowledge as correction constraints to promote the quality of solutions (generated by GM and/or DM), we propose the non-parametric Corrective Module (i.e., CM) to remove undesired artifacts from these deep modules in numerical manner. Moreover, CM actually provides a principled way to introduce domain knowledge (formulated by the objective) to correct our learning-based propagations in either FDM or PDM optimization scenarios. We first introduce a penalized reformulation of Eq. (1) as follows

$$\min_{\mathbf{u}} f(\mathbf{u}) + \phi(\mathbf{u}) + \frac{\gamma^t}{2} \|\mathbf{u} - \mathbf{u}_d^{t+1}\|^2, \quad (5)$$

where γ^t is the penalty parameter to balance the network output and domain knowledge. We leverage $\gamma^{t+1} = \eta\gamma^t$ with $\eta > 1$ to update γ . In fact, based on this formulation, original objective (i.e., $\Psi = f + \phi$ in Eq. (1)) are introduced for the correction. In particular, we actually can build diverse CM based on Eq. (5) in different optimization scenarios (i.e., FDM with whole f and ϕ and PDM with partial f), which are named as \mathcal{C}_{FDM} and \mathcal{C}_{PDM} respectively.

In detail, as for the correction of FDM, we consider the following concert scheme

$$\min_{\mathbf{u}} \tilde{f}(\mathbf{u}) + \phi(\mathbf{u}) + \frac{\gamma^t}{2} \|\mathbf{u} - \mathbf{u}_d^{t+1}\|^2, \quad (6)$$

where $\tilde{f}(\mathbf{u}) = f(\mathbf{u}_d^{t+1}) + \langle \nabla f(\mathbf{u}_d^{t+1}), \mathbf{u} - \mathbf{u}_d^{t+1} \rangle$. Exploiting proximal gradient descent scheme, we can obtain the optimal solution of Eq. (6) by optimizing the whole task-oriented fidelity and prior. Thus we define the \mathcal{C}_{FDM} as

$$\mathcal{C}_{\text{FDM}}(\mathbf{u}_d^{t+1}; \gamma^t) = \text{prox}_{\gamma, \phi}(\mathbf{u} - \frac{1}{\gamma^t} \nabla f(\mathbf{u}_d^{t+1})).$$

2. $\|\cdot\|$ is denoted as ℓ_2 -norm in this manuscript.

As for the correction of PDM, we aim to address the following optimization with partially-defined fidelity only,

$$\mathcal{C}_{\text{PDM}}(\mathbf{u}_d^{t+1}; \gamma^t) = \arg \min_{\mathbf{u}} f(\mathbf{u}) + \frac{\gamma^t}{2} \|\mathbf{u}_d^{t+1} - \mathbf{u}\|^2. \quad (7)$$

Note that f is the data fidelity and above correction usually obtains the explicit solution. Then we can solve it in closed-form to obtain the \mathcal{C}_{PDM} operation.

3.2 Training Strategies

Specifically, the most straightforward way to establish our propagative schemes is just to cascade three kinds of principled modules hierarchically in practice. Specifically, as for the image restoration and blind deblurring, we first leverage the task-based fidelity $\mathbf{u} = \arg \min_{\mathbf{u}} f(\mathbf{u}) + \frac{\gamma^t}{2} \|\mathbf{u} - \mathbf{u}^t\|^2$ to obtain a initial solution from the gradient descent of this closed-form solution. Then we construct a GM to learn the dependencies between closed-form outputs and task-specific solution, aiming to avoid complicated training phrases. Finally, we cascade three primary proposed modules repeatedly to construct our propagation to deduce the procedure of estimating the desired outputs progressively.

We actually can perform two different training strategies (i.e., greedy and joint) or their combination to optimizing the weight parameters in GM and DM. The greedy training strategies [5], [32], [48] have been exploited widely for low-level vision, aiming to train each module separately and incorporate them into our GDC propagation. Utilizing this strategy, we can train our deep modules with gradual manner to refine the output of each stage progressively. Within this training strategy, we sampled image from BSD benchmark [49] and added Gaussian noise with small interval levels to construct the training pairs, following with [32]. Moreover, we trained GM using this noised-clear training pairs, supervised by the MSE loss. As for DM, we labeled the noised images as one and the desired solution as zero and leveraged the classification criterion to train our DM. We perform greedy training on a series of image restoration and deblurring tasks. With such separate training strategies, we can obtain convergence guarantees for GDC with following control mechanisms. On the other hand, the overall scheme after direct cascade can be considered as a deep network. On the other hand, adopting the joint training [6], [7], [17] with task-oriented loss functions, we can optimize the parametric modules across stages jointly to preserve the consistency of architecture in an end-to-end manner. Furthermore, within this strategy, we collect task-oriented observations and desired task-specific solutions as our training datasets to train the architecture jointly for optical flow and rain removal tasks. Indeed, we also first perform greedy training to provide warm start and then fine-tune the parameters jointly (e.g., non-blind deconvolution).

4 PROPAGATIVE CONTROL MECHANISMS

With a unified penalty formulation, CM can correct the solutions of propagation for diverse optimization tasks (i.e., FDM and PDM) with domain knowledge. However, theoretical guarantees cannot be obtained for the whole propagation. Thus, as shown in Fig. 1, based on the correction of CM,

Algorithm 1 PCM for Fully-Defined Model

Input: The observation \mathbf{y} and necessary parameters.

Output: Latent image estimation \mathbf{u}^T .

- 1: Initialization $\mathbf{u}^0 = \mathbf{y}$.
 - 2: **for** $t = 0, \dots, T - 1$ **do**
 - 3: $\mathbf{u}_g^{t+1} \leftarrow \mathbf{u}^t + \mathcal{G}(\mathbf{u}^t; \omega_g^t)$.
 - 4: $\mathbf{u}_d^{t+1} \leftarrow \mathbf{u}_g^{t+1} + \mathcal{D}(\mathbf{u}_g^{t+1}; \omega_d^t)$.
 - 5: $\mathbf{u}_c^{t+1} \leftarrow \mathcal{C}_{\text{FDM}}(\mathbf{u}_d^{t+1}; \gamma^t)$.
 - 6: **if** $\Psi(\mathbf{u}_c^{t+1}) \leq \Psi(\mathbf{u}^t)$ **then**
 - 7: $\mathbf{v}^t \leftarrow \mathbf{u}_c^{t+1}$.
 - 8: **else**
 - 9: $\mathbf{v}^t \leftarrow \mathbf{u}^t$.
 - 10: **end if**
 - 11: $\mathbf{u}^{t+1} \leftarrow \text{prox}_{\gamma, \phi}(\mathbf{v}^t - \frac{1}{\gamma^t} \nabla f(\mathbf{v}^t))$.
 - 12: **end for**
-

we design two kinds of Propagative Control Mechanisms (i.e., PCM) as modularized techniques for whole propagative process to guide the convergent propagation towards to our desired solutions. We also obtain different convergence properties in both the FDM and PDM scenarios with PCMs.

4.1 PCM for Fully-Defined Model

Obtaining \mathbf{u}_c^{t+1} from certain correction of CM and facing with the convergence of general FDM, we propose the optimality checking mechanism to control output \mathbf{u}_c^{t+1} based on the objective function's monotonicity. Actually, obtaining $\Psi(\mathbf{u}_c^{t+1})$ from CM, we choose the optimal objective value \mathbf{v}^t through explicitly comparing $\Psi(\mathbf{u}^t)$ with $\Psi(\mathbf{u}_c^{t+1})$. Then the final solution of \mathbf{u}^{t+1} can be computed by optimizing concrete FDM with temporary variable \mathbf{v}^t , using proximal-gradient scheme. The whole GDC scheme for FDM with PCM is summarized in Alg. 1.

As PCM for FDM, we also assume that f has the Lipschitz constant L , ϕ is a nonsmooth and nonconvex function with lower semi-continuity, $\Psi(\mathbf{x})$ is coercive. Exploiting with Proposition 1, it can verify the sufficient descent property of objectives directly and Alg. 1 can converge to the critical points.

Proposition 1. (Critical Point Convergence of PCM for FDM) *Let $\{\mathbf{u}^t, \mathbf{v}^t\}$ be the sequences generated by Alg. 1. With PCM, we have the following conclusions: (1) The objective function satisfies $\Psi(\mathbf{u}^t) \geq \Psi(\mathbf{u}^{t+1}) + \beta^t d_t$, where d_t denotes the distance between output \mathbf{u}^{t+1} and the selected \mathbf{v}^t with $\beta^t > 0$. (2) Any accumulation points (denoted as \mathbf{u}^*) of $\{\mathbf{u}^t\}$ are the critical points of Eq. (1), i.e., they satisfy $\mathbf{0} \in \partial \Psi(\mathbf{u}^*)$.*

4.2 PCM for Partially-Defined Model

Considering complex low-level vision tasks, it is challenging to introduce explicit priors to formulate the distribution (e.g., the complicated statistics of rain streaks). We also introduce another PCM to control the propagation of PDM with explicit partially-defined fidelity and the output of CM \mathbf{u}_c^{t+1} . We define the optimality checking condition is $\|\nabla f(\mathbf{u}_c^{t+1})\| \leq L$. Specifically, targeting to the checking of latent solution \mathbf{u}_c^{t+1} , we define final output \mathbf{u}^{t+1} as $\mathbf{u}^{t+1} \leftarrow \mathbf{u}_c^{t+1}$ if $\|\nabla f(\mathbf{u}_c^{t+1})\| \leq L$ and $\mathbf{u}^{t+1} \leftarrow \mathbf{u}^t$ otherwise.

With Proposition 2, the fixed point convergence of this PCM for PDM can be guaranteed. Alg. 2 summarizes the whole GDC with PCM scheme for PDM. In this way, GDC is more flexible to extend more complex low-level vision applications, which may have difficulty in formulating the prior information explicitly.

Algorithm 2 PCM for Partially-Defined Model

Input: The observation \mathbf{y} and necessary parameters.

Output: Latent image estimation \mathbf{u}^T .

```

1: Initialization  $\mathbf{u}^0 = \mathbf{y}$ .
2: for  $t = 0, \dots, T - 1$  do
3:    $\mathbf{u}_g^{t+1} \leftarrow \mathbf{u}^t + \mathcal{G}(\mathbf{u}^t; \boldsymbol{\omega}_g^t)$ .
4:    $\mathbf{u}_d^{t+1} \leftarrow \mathbf{u}_g^{t+1} + \mathcal{D}(\mathbf{u}_g^{t+1}; \boldsymbol{\omega}_d^t)$ .
5:    $\mathbf{u}_c^{t+1} \leftarrow \mathcal{C}_{\text{PDM}}(\mathbf{u}_d^{t+1}; \gamma^t)$ .
6:   if  $\|\nabla f(\mathbf{u}_c^{t+1})\| \leq L$  then
7:      $\mathbf{u}^{t+1} \leftarrow \mathbf{u}_c^{t+1}$ .
8:   else
9:      $\mathbf{u}^{t+1} \leftarrow \mathbf{u}^t$ .
10:  end if
11: end for
    
```

Proposition 2. (Fixed Point Convergence of PCM for PDM) Let $\{\mathbf{u}^t\}$ to be the sequence generated by Alg. 2 and f to be continuous differentiable with Lipschitz constant L . Denoted \mathcal{T}_G and \mathcal{T}_D as the operators of GM and DM, assuming $\|\mathcal{T}_D \circ \mathcal{T}_G(\mathbf{u}^t) - \mathbf{u}^t\| \leq \sqrt{c}/\gamma^t$ for any input \mathbf{u}^t is satisfied, where $c > 0$, we conclude that sequence $\{\mathbf{u}^t\}$ converges to a fixed-point.

5 ARCHITECTURE AUGMENTATION STRATEGIES

To improve the performance of propagation, we investigate two Architecture Augmentation Strategies (i.e., AAS) include Architecture Normalization (i.e., AN) and Architecture Search (i.e., AS) to enhance the stability of propagation and discover automated task-specific architectures respectively. As shown in Fig. 1, AASs are performed for deep architectures, where we use \mathcal{N} , $\boldsymbol{\omega}$ to denote these deep modules and weights, i.e., $\mathcal{N} := \{\mathcal{G}, \mathcal{D}\}$ and $\boldsymbol{\omega} := \{\boldsymbol{\omega}_g, \boldsymbol{\omega}_d\}$.

5.1 Architecture Normalization

In order to avoid large oscillations generated by manually designed architectures and enhance the stability of propagation, architecture normalization is proposed, investigating their contraction property of these architectures (i.e., \mathcal{N}). The contraction property of \mathcal{N} indicates that $\|\mathcal{N}(\mathbf{u}_1) - \mathcal{N}(\mathbf{u}_2)\| \leq \delta \|\mathbf{u}_1 - \mathbf{u}_2\|$ with Lipschitz constant $\delta < 1$. In this way, if architecture \mathcal{N} satisfies this property, the inequality $\|\mathcal{N}(\mathbf{u}^{t+1}) - \mathcal{N}(\mathbf{u}^t)\| / \|\mathbf{u}^{t+1} - \mathbf{u}^t\| \leq \delta$ could be obtained to guarantee the stability of propagation.

Indeed, above inequality can be converted as to control the largest singular values of \mathcal{N} . Since it is well known that its Lipschitz norm $\|\mathcal{N}\|_{\text{Lip}}$ is just the largest singular value of weight matrix [50]. In nutshell, architecture normalization controls the largest singular values of weights per layer to enforce $\|\mathcal{N}\|_{\text{Lip}}$ from above 1. For instance, we define that \mathcal{N} is a network with K convolution layers. We normalize the weights $\boldsymbol{\omega}^k$ of the k -th layer to achieve

$$\max_{\mathbf{u}^t \neq \mathbf{0}} \|\boldsymbol{\omega}^k \mathbf{u}^t\| / \|\mathbf{u}^t\| = \max_{\|\mathbf{u}^t\| \leq 1} \|\boldsymbol{\omega}^k \mathbf{u}^t\| \leq (\delta)^{\frac{1}{K}}, \quad (8)$$

where we define the constant $\delta \in (0, 1]$ and above equation implies that $\|\mathcal{N}\|_{\text{Lip}} \leq \delta$. We utilize one matrix power accelerated iteration method [51] with a random Gaussian vector \mathbf{z} to perform AN, i.e.,

$$\varrho(\boldsymbol{\omega}) = \mathbf{z}^\top (\boldsymbol{\omega} \boldsymbol{\omega}^\top)^2 \mathbf{z} / (\|\boldsymbol{\omega}^\top \mathbf{z}\| \|\boldsymbol{\omega} \boldsymbol{\omega}^\top \mathbf{z}\|), \quad (9)$$

We leverage $\tilde{\boldsymbol{\omega}} = \boldsymbol{\omega} / \varrho(\boldsymbol{\omega})$ to update the parameters of each layer of deep modules at the forward propagation. As shown in the AN part of Fig. 1, the largest singular value of \mathcal{N} with (w/o) AN is much smaller than \mathcal{N} without (w/o) AN.

Different from the work [50] for the stabilization training of discriminator, we learn from the basic strategy locally of this work to obtain convergent task-specific solutions and stable propagations. Furthermore, AN can be utilized in the joint training of whole architecture. We also demonstrate that AN guarantees the fixed-point convergence for convex fully-defined objectives (e.g., image deconvolution, image denoising and optical flow estimation) in Proposition 3.

Proposition 3. (Fixed-point Convergence with AN) Let $\{\mathbf{u}^t\}$ to be the sequence generated by GDC with AN. Assuming f is ρ -strong convex with Lipschitz constant L , the sequence $\{\mathbf{u}^t\}$ converges to a fixed-point if $(1 + \delta_d)(1 + \delta_g) < \frac{\rho + L}{|\rho - L|}$, where δ_g and δ_d denote the Lipschitz constants of GM and DM.

5.2 Architecture Search

As aforementioned, GM and DM in our GDC are CNN-based networks. However, manual design of these deep modules is a challenging task, requiring extensive architecture engineering and subtle adjustments. Inspired by the success of NAS in high-level vision field [43], we propose an architecture search strategy by introducing a compact search space and proposing a differentiable NAS strategy to discover one task/data-specific architecture \mathcal{N} (i.e., GM or DM) automatically for low-level vision.

It is worth emphasizing that, we propose an effective task-oriented search space for low-level vision, instead of utilizing the primitive operators [43] (e.g., normal 3×3 convolution and max pooling). The search space is a set that contains the possible operators as the selections for designing task-specific \mathcal{N} , which includes

- 3×3 Dilated Convolution (3-DC)
- 3×3 Residual Blocks (3-RB)
- 3×3 Dense Blocks (3-DB)
- Spatial Attention (SA)
- 5×5 Dilated Convolution (5-DC)
- 3×3 Residual Blocks (5-RB)
- 5×5 Dense Blocks (5-DB)
- Channel Attention (CA)

The above operations [52], [53] have been demonstrated to deal with a series of low-level vision tasks effectively, which also guarantee the generalization and adaption ability of proposed AS to discover proper architectures for GM or DM to address diverse low-level vision tasks.

Then we consider a differentiable search optimization strategy to perform AS under GDC scheme, which is

$$\begin{aligned} \min_{\boldsymbol{\alpha}} \quad & \mathcal{L}_{\text{val}}(\mathcal{N}(\mathbf{u}; \boldsymbol{\omega}^*(\boldsymbol{\alpha}))) \\ \text{s.t.} \quad & \boldsymbol{\omega}^*(\boldsymbol{\alpha}) = \arg \min_{\boldsymbol{\omega}} \mathcal{L}_{\text{train}}(\mathcal{N}(\mathbf{u}; \boldsymbol{\omega}(\boldsymbol{\alpha}))), \end{aligned} \quad (10)$$

where $\mathcal{L}_{\text{train}}$ and \mathcal{L}_{val} denote task-oriented losses on the training and validation dataset. $\boldsymbol{\alpha}$ represents the relaxation weights of architecture, following with [43].

TABLE 1

Summary of the optimization formulations for low-level vision tasks. \mathbf{B} denotes the inverse wavelet transform and is utilized to compute the hyper-Laplacian prior [21].

Types	Tasks	$f(\mathbf{u})$	$\phi(\mathbf{u})$
	Deconvolution	$\ \mathbf{u} \otimes \mathbf{k} - \mathbf{y}\ ^2$	$\ \mathbf{B}^T \mathbf{u}\ _1$
	Optical Flow	$\ \mathbf{I}_1(\mathbf{u}) - \mathbf{I}_0\ ^2$	$\ \nabla \mathbf{u}\ _1$
FDM	Deblurring	$\ \mathbf{u} \otimes \mathbf{k} - \mathbf{y}\ ^2$	$\ \mathbf{B}^T \mathbf{u}\ _{0.8}$
	Interpolation	$\ \mathbf{u} \odot \mathbf{M} - \mathbf{y}\ ^2$	$\ \mathbf{B}^T \mathbf{u}\ _{0.8}$
	Smoothing	$\ \mathbf{u} - \mathbf{y}\ ^2$	$\ \mathbf{B}^T \mathbf{u}\ _0$
PDM	Rain Removal	$\ \mathbf{u} - \mathbf{y}\ ^2$	-

In detail, as shown in Fig. 1, we leverage the basic block (i.e., search cell) to simplify the search process of concrete architecture. The basic cell can be implemented as a directed acyclic graph, where the graph including one node of input, a sequence of four inner nodes and one node of the output. We define that each nodes are connected fully to the following nodes and last output. Specifically, each edge of cell represents the weighted sum of possible operators from search space. Inner node represents the sum of all edges from previous nodes. The final output is performed by the sum of features from previous nodes.

6 APPLICATIONS

In this section, we demonstrate how to apply GDC to address a series of low-level vision applications. In Table. 1, we summary the clear energy formulations of low-level vision tasks that considered in this paper.

6.1 GDC with Fully-Defined Model

FDM can observe both the fidelity f and explicit prior ϕ in Eq. (1), where physical rules from f and regularization from ϕ provide task-oriented domain knowledge for diverse tasks. We apply GDC for five low-level vision applications (i.e., deconvolution, optical flow, deblurring, interpretation and smoothing) with clear FDMs. Note that, for particular task, we would like to follow existing works to choose the prior term, thus can obtain relatively fair comparisons.

Non-blind Deconvolution: The purpose of non-blind deconvolution is to restore the latent images from corrupted observations with known blur kernels. We formulate the specific case of Eq. (1) for non-blind deconvolution as $f(\mathbf{u}) = \|\mathbf{u} \otimes \mathbf{k} - \mathbf{y}\|^2$ and $\phi(\mathbf{u}) = \|\mathbf{B}^T \mathbf{u}\|_1$, where $\mathbf{u}, \mathbf{y}, \mathbf{k}$ and \otimes are corresponding to the latent image, observation, blur kernel and convolution operator respectively. We follow the related works [25] to adopt the ℓ_1 -norm. For GM, we establish a residual network with seven convolution layers and six ReLU blocks, which is plugged behind each convolution layers. The DM is constructed as a standard CNN-based classifier [28] to promote the latent solutions. Particularly emphasized that, we also use the same architectures to deal with the following image restoration tasks.

Optical Flow: Optical flow which relates to the pixel correspondence across two consecutive frames is aroused by spatial motions of any points in the related images. Specifically, we denote the optical flow as \mathbf{u} and formulate the

fidelity as $f(\mathbf{u}) = \|\mathbf{I}_1(\mathbf{u}) - \mathbf{I}_0\|^2$ and $\phi(\mathbf{u}) = \|\nabla \mathbf{u}\|_1$, where $\mathbf{I}_0, \mathbf{I}_1$ are two consecutive frames and $\mathbf{I}_1(\mathbf{u})$ denotes the estimated locations of previous \mathbf{I}_0 warped by \mathbf{u} . The fidelity imposes the pixel correspondence of images and penalize the brightness constancy between two frames. Moreover, the widely used TV regularization [54] for optical flow is introduced to penalize the high variants of flow for local smooth. Instead of utilizing the homologous network for image restoration, we develop a task-specific GM to estimate the optical flow by introducing the pixel correspondence in the pyramid feature domain.

Blind Deblurring: Blind deblurring includes estimating the blur kernel and recovering the sharp image from a blurred input. Here we demonstrate how to incorporate GDC into a kernel estimation process to nest the blind-deblurring process. We leverage the similar fidelity of non-blind deconvolution to model relations of image pairs in gradient domain, where \mathbf{u}, \mathbf{y} denote gradients of solutions and corruptions in this application. The nonconvex hyper-Laplacian with $\ell_{0.8}$ -norm, is proposed in [55] and used as one regularization, aiming to model the distribution at gradient domain better and preserve clear structures for this challenging task. We train the GM with noised images as inputs and the clear gradients (including the horizontal and vertical gradient) as labels. Then we just adopt most normally utilized frameworks (e.g., [20], [56]) to estimate blur kernel \mathbf{k} at t -th iteration $\mathbf{k}^{t+1} = \arg \min_{\mathbf{k} \in \Delta} \frac{1}{2} \|\mathbf{u}^{t+1} \otimes \mathbf{k} - \mathbf{y}\|^2 + \mu \|\mathbf{k}\|^2$, where $\Delta = \{\mathbf{k} | \mathbf{1}^T \mathbf{k} = 1, [\mathbf{k}]_i \geq 0\}$ is corresponding to the complex constraint, μ is a parameter for accommodation and \mathbf{u}^{t+1} is the output of t -th iteration. We also introduce the classical coarse-to-fine strategy [20], [36] for kernel estimation. With the guide of PCM, iterative behaviors of blind deblurring can be guaranteed.

Image Interpolation: The main objective of image interpolation is to restore partially invisible measurements, which are corrupted by some masks, such as pixel missing and text. When using our paradigm to address this ill-posed tasks, the prominent difference with non-blind deconvolution is fidelity term, which can be formulated as $f(\mathbf{u}) = \|\mathbf{u} \odot \mathbf{M} - \mathbf{y}\|^2$, where \odot represents the pixel multiplication and \mathbf{M} denotes occluded corrections. We also utilize hyper-Laplacian with $\ell_{0.8}$ -norm as the regularization.

Edge-preserved Smoothing: Edge-preserved smoothing attempts to extract dominant structures of observations and eliminate undesired textures and noises. We construct the FDM formulation of this application through changing the fidelity formulation with the desired smooth solution \mathbf{u} and the observation \mathbf{y} . As for this application, we establish the fidelity as $f(\mathbf{u}) = \|\mathbf{u} - \mathbf{y}\|^2$ and build widely used ϕ as ℓ_0 -norm prior [35] to smooth the textures, which provide the concrete model of Eq. (1).

6.2 GDC with Partially-Defined Model

PDM only observes the fidelity f explicitly but without information on the prior ϕ , since it remains challenging to introduce proper and effective priors to model precise distribution for complex vision tasks. Actually, rain removal is a representative task due to the difficulty of introducing priors to formulate the complex statistics of rain streaks.

Rain Removal: Recovering the rain-degraded images is a challenging but crucial task for the outdoor visual

TABLE 2
Averaged PSNR of stacked modules on Levin *et al.* [57]/BSD68 [2].

σ	G	GD	GC	GDC
1%	34.81/29.51	34.89/29.79	34.86/29.80	34.90/29.79
2%	32.12/27.84	32.26/27.91	32.41/27.85	32.36/28.00
3%	30.35/26.88	30.51/26.83	30.52/26.83	30.69/26.97

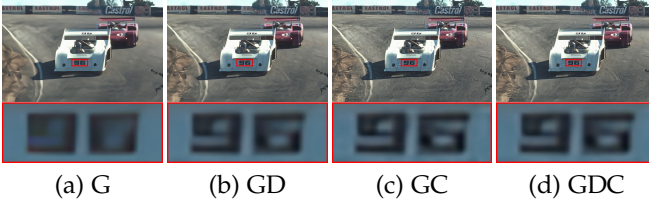


Fig. 2. The visual results of series schemes under 3% noise level.

scenario, aiming to remove rain streaks and recover details simultaneously. We leverage PDM to characterize the rain removal task based on Alg. 2. Considering rain streaks can be regarded as a category of signal-dependent noises, we define the fidelity term as $\|\mathbf{u} - \mathbf{y}\|^2$, aiming to persevere the structure of latent images. Actually, we perform AS to discover the concrete GM and DM for rain removal respectively, where GM consists four search cells and DM contains two cells. Moreover we also provide the manual designed GDC scheme. As for GM, we adopt the chained architecture to propagate the feature with 3×3 residual block, 3×3 dense block, 3×3 dilated convolution and attentions progressively. As for the DM, we introduce the pre-trained DM (with similar architecture for deconvolution). Both schemes are trained jointly with Rain800 [39].

7 ABLATION STUDY

In this section, we investigate the properties of these propagative modules, the efficiency of PCM and AAS on non-blind deconvolution task.

Foundational Modules Evaluation: In this part, the properties of each basic module are carefully discussed. In Table. 2, we reported the experimental results of different cascade schemes (i.e., G, GC, GD and GDC) under diverse Gaussian noise levels. σ denotes the percent form of Gaussian noise level. GM obtained considerable performances and GC achieved better quantitative results under the disturbance of small noise particularly. Although GDC obtained similar performances with GC, but the visual result of Fig. 2 showed that GDC had less artifacts than GC.

We also illustrated the performances of joint training for these schemes, denoted this strategy as “J”, where we reported quantitative results in Table. 3. All these schemes with joint training strategy improved the performances greatly compared with greedy training. We can see that $(GDC)_J$ has better performances under the strong noise. $(GC)_J$ obtained the satisfied result under small noise level. On the other hand, visual results of different networks with joint training are shown in Fig. 3. $(GDC)_J$ obtained more favorably visual and quantitative results than other networks, especially under strong noises (e.g., 5%).



Fig. 3. The visual results of joint training under 5% noise level.

TABLE 3
The quantitative results of joint training on Levin *et al.* [57]/BSD68 [2].

σ	G_J	$(GC)_J$	$(GDC)_J$
1%	35.45/30.07	35.57/30.11	35.51/30.09
2%	32.57/28.28	32.73/28.30	32.75/28.25
3%	30.86/27.27	31.08/27.28	31.06/27.15
5%	28.76/25.30	28.86/25.92	28.94/26.06
10%	26.04/24.35	26.05/24.43	26.25/24.57

PCM Evaluation: We then evaluated the effectiveness of PCM for this FDM task. As shown in Fig. 4, we compared the iteration behaviors of GC and GC_{PCM} , where we exploited the reconstruction error to stop iterations automatically. The curves of original GC were oscillated and could not satisfy the automatic stop condition through finite numbers of iterations. GC_{PCM} obtained more stable outputs with less iterations that demonstrates the efficiency of our proposed PCM.

AAS Evaluation: As for AN, we adopted GC scheme to verify the efficiency and compare the properties of our architectures \mathcal{N} (i.e., GM in this scenario) with (w/) and without (w/o) AN in Fig. 5. The subfigure (a) and subfigure (b) plot the frequency of $\|\mathcal{N}(\mathbf{u}^{t+1}) - \mathcal{N}(\mathbf{u}^t)\| / \|\mathbf{u}^{t+1} - \mathbf{u}^t\|$, where the ratio for GM w/ AN is much smaller than GM w/o AN. Thereby, these experimental results justified the effectiveness of AN. Furthermore, we also analyzed the final AS-based architectures for rain removal task. The Fig. 6 shows the final searched architectures of GM and DM respectively. GM contains more residual blocks and dilated convolution with small receptive fields, which is reasonable, demonstrated by previous manually designed works [38], [41]. DM consists many dilated convolutions with large receptive fields, tending to capture more contextual information of observations. In this way, these results indicated the significance of AS to discover the task-specific architectures.

8 EXPERIMENTAL RESULTS

In this section, a range of experimental results have demonstrated the superiority of GDC series methods on a various low-level vision applications.

Non-blind Deconvolution: We compared our method against state-of-the-art approaches, including FISTA [25], FTVD [62], HL [21], EPLL [60], FDN [58], IRCNN [32], MSWNNM [61], MEDAEP [29] and GLRA [37]. We conducted the comparisons on widely used Levin *et al.* [57]

TABLE 4
Quantitative results (PSNR/SSIM) about non-blind deconvolution compared with state-of-the-art methods.

Benchmarks	Methods	[25]	[21]	[21]	[60]	[58]	[32]	[61]	[29]	[37]	Ours
Levin <i>et al.</i>	PSNR	30.63	29.38	31.18	32.65	33.59	34.61	34.97	19.77	19.75	35.57
	SSIM	0.82	0.88	0.85	0.91	0.93	0.93	0.93	0.46	0.51	0.95
BSD68	PSNR	26.97	28.31	26.93	28.76	29.49	29.83	29.86	20.11	17.61	30.11
	SSIM	0.69	0.78	0.76	0.79	0.89	0.85	0.84	0.45	0.43	0.86

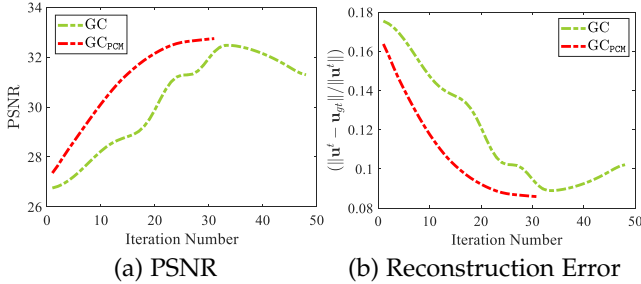


Fig. 4. Convergence analysis of GC and GC_{PCM}.

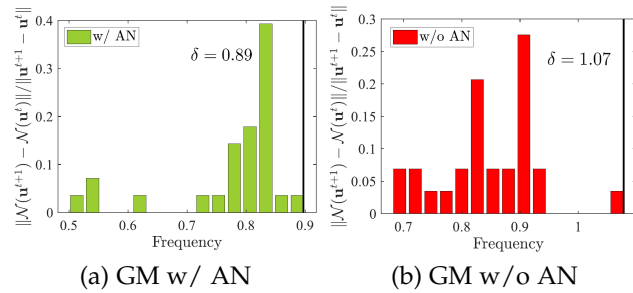


Fig. 5. The frequency statistics of $\frac{\|\mathcal{N}(\mathbf{u}^{t+1}) - \mathcal{N}(\mathbf{u}^t)\|}{\|\mathbf{u}^{t+1} - \mathbf{u}^t\|}$ for GM w/ and w/o AN.

and BSD68 [2] under 1% noise. As shown in Fig. 7, our method is effective in preserving the clear structure and generating perceptually-pleasant outputs. We also reported the average quantitative comparison in terms of PSNR and SSIM in Table. 4. Our GDC with AN using joint training, performed favorably against a series of conventional and data-driven deconvolution methods.

Optical Flow Estimation: We compared our method with state-of-the-art methods for optical flow estimation, including FlowNet [63], FlowNet2 [7], SpyNet [64], Liteflownet [8] and PWCNet [6]. All methods were trained by FlyingChairs [63] and FlyingThings3D [7] dataset. Techni-

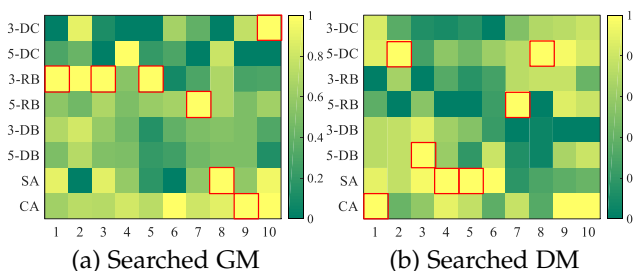


Fig. 6. Heatmaps about basic candidate operators of GM and DM at the last search epoch. The final architectures are indicated by red boxes.

TABLE 5
Average EPE of GDC compared with other optical flow estimation methods on four optical flow benchmarks. The value in parentheses is FI-all, meaning the percentage of outliers averaged over all pixels.

Methods	Sintel clean	Sintel final	KITTI 2012	KITTI 2015
[63]	3.04	4.60	5.79	11.49 (44.09%)
[64]	4.12	5.57	5.79	-
[7]	2.02	3.54	4.01	9.94 (28.02%)
[8]	2.48	4.04	4.00	10.39 (28.50%)
[6]	2.55	3.93	4.14	10.35 (33.67%)
Ours	2.28	3.74	4.92	11.60 (31.69%)

cally, as for the architecture of GM, we first constructed pyramid encoders to extract the multi-scale feature of both frames. By utilizing the warping technique and correlation layers, which have been leveraged in [6], [63] to calculate the correlation of corresponding pixels, we imposed this consistency in the feature domain and established a residual CNN to estimate optical flow in different scales. Behind each level of GM, we adopted the CM to regularize the estimated flow. In Table. 5, we provided average End-point Error (i.e., EPE) on different benchmarks compared with state-of-art methods. We illustrated that our framework are superior to all other lightweight networks [6], [8], [64] on the Sintel final [59]. Our method also obtained the significant results (FI-all) on the KITTI [9]. It is clear to see that the generated flows of our method have lesser artifacts and sharper boundaries in Fig. 8. Our method is better for capturing small motion information (e.g., hand movement).

Image deblurring: First of all, we evaluated our methods with other deblurring competitors including traditional deblurring methods such as NSM [65], CASP [1], Levin *et al.* [66], TV [14] and state-of-the-art methods such as patch prior [36], dark-channel prior [22], extreme-channel prior [23], discriminative prior [67] on two synthetic datasets, i.e., Levin *et al.*'s dataset [57] and Sun *et al.*'s dataset [36]. To compare other blind deblurring approaches fairly, we introduced the non-blind deconvolution method [60] to estimate final latent images. In Table. 6, GC advanced state-of-the-art significantly on Levin *et al.*'s dataset and costed the shortest running time notably. GDC had the best PSNR result on the challenging Sun *et al.* [36]'s dataset, but it also consumed much longer time because the inference of DM. In Fig. 9, we depicted the visual comparisons of our schemes together with the best two approaches in above table (i.e., Yan *et al.* [23] and Pan *et*

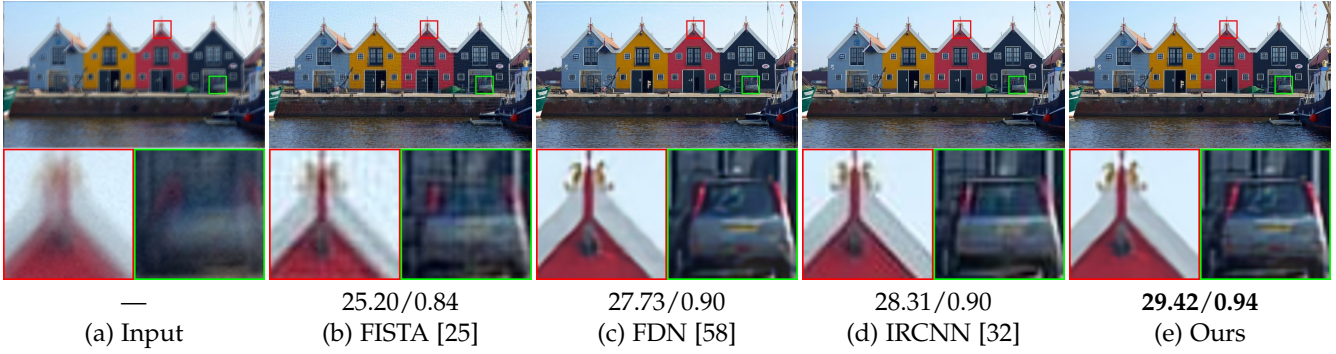


Fig. 7. Non-blind deconvolution comparisons with other competitive methods. Quantitative metrics (PSNR/SSIM) are reported below each image.

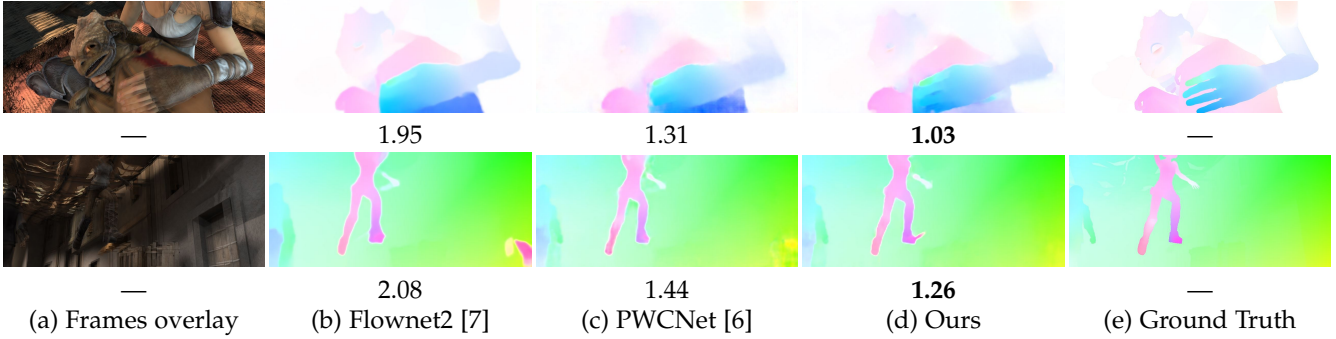


Fig. 8. Optical flow comparisons on two frames from Sintel [59]. Quantitative metrics (End-point Error) are reported below each result.

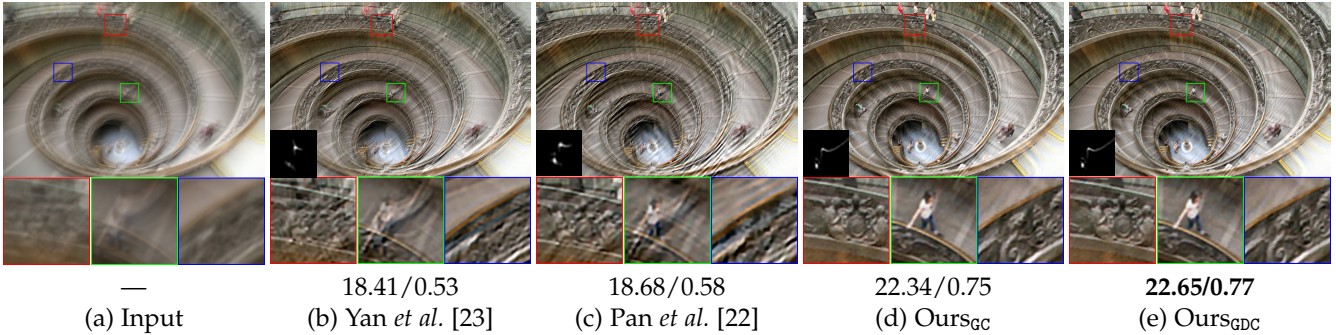


Fig. 9. Deblurring comparisons on a synthetic image. Quantitative metrics (PSNR/SSIM) are reported below each image.

TABLE 6

Quantitative results about image deblurring on image set (Levin et al. [57] / Sun et al. [36]), lower ER is better.

Methods	PSNR	SSIM	ER	TIME
[65]	24.87/22.92	0.74/0.75	2.05/5.01	23.78/126.78
[1]	28.01/28.08	0.86/0.79	1.25/1.84	37.45/684.73
[66]	29.03/24.90	0.89/0.80	1.40/3.28	41.77/392.27
[14]	29.27/25.45	0.88/0.78	1.35/13.7	113.70/1013.52
[36]	29.71/29.48	0.90/0.85	1.32/1.73	209.47/1754.09
[22]	29.78/29.60	0.89/0.84	1.33/1.43	102.60/215.66
[23]	29.87/29.57	0.89/0.83	1.32/1.45	29.56/172.55
[67]	29.76/29.60	0.89/0.83	1.31/1.41	67.40/127.17
Ours _{Gc}	30.35/29.65	0.91/0.84	1.21/1.41	6.21/46.33
Ours _{GDC}	30.30/29.70	0.92/0.84	1.37/1.80	10.79/194.9

TABLE 7

Average image interpolation results (PSNR/SSIM) on CBSD68 [2].

Mask	[2]	[68]	[69]	Ours
20%	38.23/0.96	35.20/0.96	37.55/0.97	38.78/0.98
80%	27.64/0.65	24.92/0.70	27.31/0.80	27.77/0.82

al. [22]). Obviously, Yan et al. [23] and Pan et al. [22] could not estimate accurate kernel on this synthetic blurry image. GDC scheme could generate more visual-pleasant content and clear structure. Moreover, we validated the advantage of our schemes on real-world blurry images with other state-of-the-art methods in Fig. 10. GDC could remove artifacts effectively and estimated more accurate blur kernel than other methods. We also conducted the comparison with a blurred text image. Obviously, GDC generated more contextual details and recovered better structural patterns than other schemes.

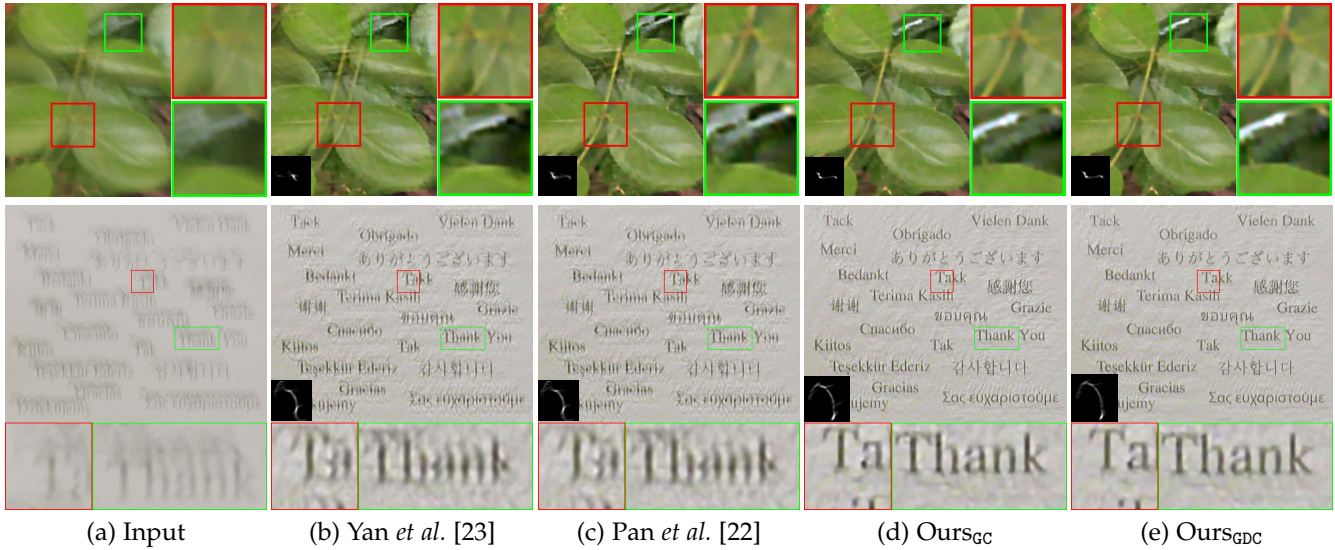


Fig. 10. Deblurring comparisons on the herculean real-world blurred observations.

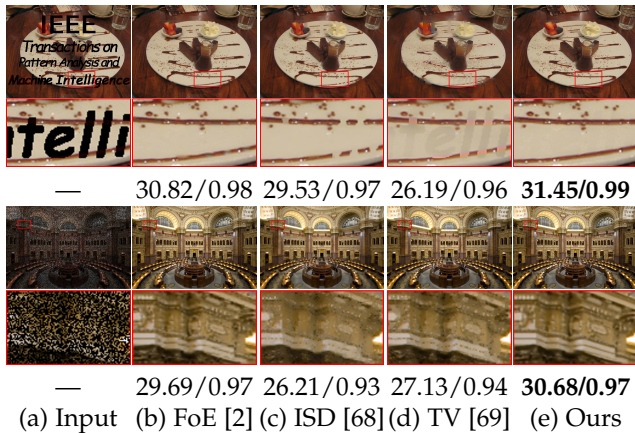


Fig. 11. Interpretation comparisons with different masks (i.e., text and 60% pixels missing). Quantitative metrics are listed below each image.

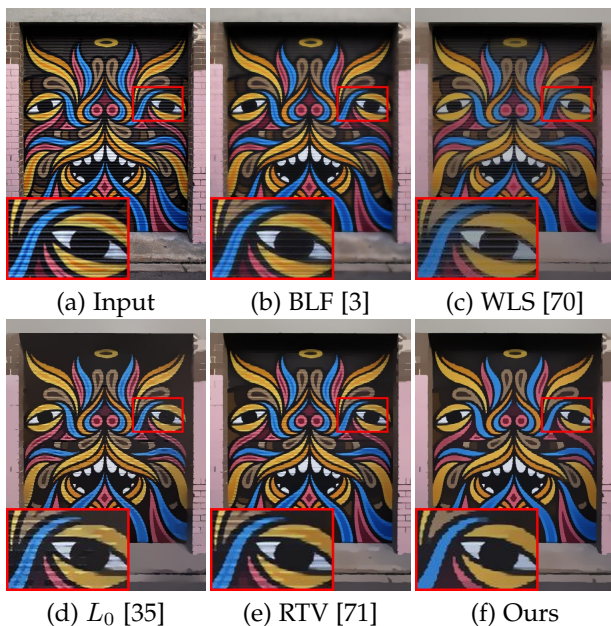


Fig. 12. Smoothing comparisons on an example with horizontal textures.

TABLE 8
Quantitative results (PSNR/SSIM) about rain removal on Rain800 [39].

Metrics	[38]	[39]	[40]	[41]	[42]	[16]	Ours _{MD}	Ours _{AS}
PSNR	22.24	24.09	22.27	21.14	26.31	24.59	27.65	28.14
SSIM	0.78	0.84	0.79	0.78	0.86	0.82	0.87	0.88

Image Interpolation: To analysis the superiority of our schemes for this application, we compared GDC against other state-of-the-art competing methods including FoE [2], ISD [68] and TV [69] on two kinds of masks (e.g., text and random masks of pixel missing). We reported the average quantitative results on CBSD68 dataset [2] in Table. 7. We conducted the experiment under 20% and 80% of pixel missing. GDC scheme achieved best scores under diverse missing rates. In Fig. 11, our GDC achieved the better visual and quantitative results compared with other interpolation methods. It is obvious to observe that TV [69] generated more pixel missing regions. ISD [68] and FoE [2] restored the most regions of images. However these methods yielded much blurry results.

Edge-Preserved Smoothing: Edge-preserved smoothing involves two parts, i.e., the undesired textual removal and the structure preservation. We conducted this comparison with state-of-the-art competitors, such as BLF [3], WLS [70], L_0 [35] and RTV [71]. In Fig. 12, we depicted their visual results with a representative example, which is a rolling door with horizontal textures. Furthermore, it is clear to see that traditional methods such as BLF [3], L_0 [35] preserved the dominant boundaries, but remained obvious horizontal textures. RTV [71] kept the boundaries considerably better, though the result also has some trivial lines. Our GC scheme removed the most undesired artifacts effectively and obtained the smoother visual performance.

Rain Removal: We proposed a manually designed GDC scheme, denoted as “MD”. Emphatically, we also introduced AS to address this complicated rain removal task. We competed our schemes against other state-of-the-art algorithms, including JORDER [38], RSCAN [39], NLEDN [40] and

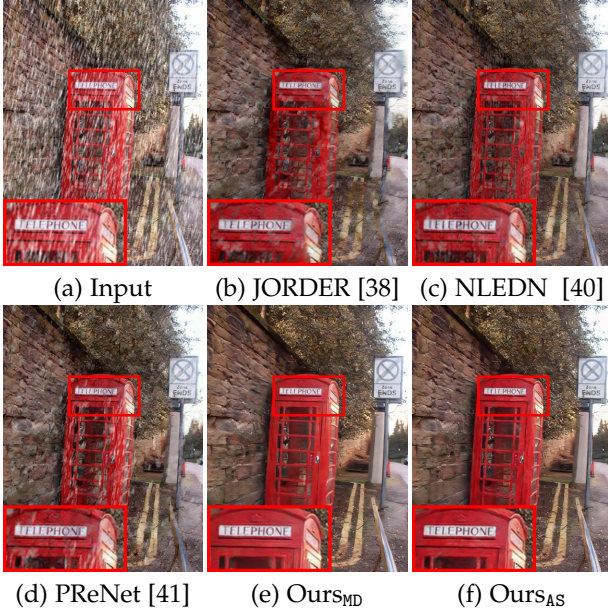


Fig. 13. Rain removal comparisons with other competitive methods.

recently proposed methods (PReNet [41], RCDNet [16]) and HiNAS [42]. As reported in Table. 8, our methods achieved the best quantitative results in term of PSNR and SSIM measurements, which also demonstrate the flexibility and efficiency of our AS for GDC. We also show our visual performance by selecting one typical challenging image from Rain800, shown in Fig. 13. JORDER [38] and NLEDN [40] removed major rain streaks but remained undesired artifacts. The result of PReNet [41] also remained residue rain streaks. Both GDC schemes obtained clear backgrounds.

9 CONCLUSIONS

This paper provided a unified optimization-inspired image propagation framework for diverse low-level vision tasks, aggregating generative manner, discriminative metric and domain knowledge correction principles from “optimization learning” perspective. We introduced two propagative control mechanisms to guarantee convergent propagations for both fully- and partially- defined optimization models. We also proposed two architecture augmentation strategies (i.e., normalization and architecture search) to enhance the stability of propagations and discover task-specific architecture respectively. Extensive experimental results demonstrated the high flexibility and effectiveness of our framework for a series of low-level vision applications.

ACKNOWLEDGMENTS

This work was supported by the National Natural Science Foundation of China (Nos. 61922019, 61672125, 61733002 and 61572096), the Youth Tiptop Talent project in Liaoning Province (XLYC1807088) and the Fundamental Research Funds for the Central Universities.

APPENDIX

Proof for Proposition 1

Proof. The following proof demonstrates the critical point convergence for GDC scheme with PCM for FDM. After the

checking of PCM, the step 11 of Alg. 1 implies that $\mathbf{u}^{t+1} \leftarrow \text{prox}_{\gamma, \phi}(\mathbf{v}^t - \frac{1}{\gamma^t} \nabla f(\mathbf{v}^t))$. Thus we have

$$\mathbf{u}^{t+1} \in \arg \min_{\mathbf{u}} \left\{ \phi(\mathbf{u}) + \frac{\gamma^t}{2} \|\mathbf{u} - \mathbf{v}^t + \frac{1}{\gamma^t} \nabla f(\mathbf{v}^t)\|^2 \right\}.$$

Subsequently, the above equation yields

$$\phi(\mathbf{u}^{t+1}) \leq \phi(\mathbf{v}^t) - \frac{\gamma^t}{2} d_t - (\nabla f(\mathbf{v}^t))^\top (\mathbf{u}^{t+1} - \mathbf{v}^t), \quad (11)$$

where $d_t = \|\mathbf{u}^{t+1} - \mathbf{v}^t\|^2$. Considering the convexity and the Lipschitz smooth properties of f , the following

$$f(\mathbf{u}^{t+1}) \leq f(\mathbf{v}^t) + (\nabla f(\mathbf{v}^t))^\top (\mathbf{u}^{t+1} - \mathbf{v}^t) - \frac{L}{2} d_t, \quad (12)$$

holds. Summing up Eq. (11) and Eq. (12), we can have $\Psi(\mathbf{u}^t) \geq \Psi(\mathbf{u}^{t+1}) + \beta^t d_t$ with $\beta^t = \frac{L + \gamma^t}{2}$. If $\mathbf{v}^t \leftarrow \mathbf{u}^t$, the first conclusion in Proposition 1 is completed, else we have $\Psi(\mathbf{v}^t) = \Psi(\mathbf{u}_c^{t+1}) \leq \Psi(\mathbf{u}^t)$. Obviously, we obtain the sufficient descent property. This implies that $\|\mathbf{u}^{t+1} - \mathbf{v}^t\| \rightarrow 0$ as $t \rightarrow \infty$. As the updated step after optimality checking of PCM is computed by proximal gradient scheme in Alg. 1), the optimal condition $0 \in \partial \phi(\mathbf{u}^{t+1}) + \gamma^t(\mathbf{u}^{t+1} - \mathbf{v}^t + \frac{1}{\gamma^t} \nabla f(\mathbf{v}^t))$ implies

$$-\gamma^t(\mathbf{u}^{t+1} - \mathbf{v}^t) - \nabla f(\mathbf{v}^t) + \nabla f(\mathbf{u}^{t+1}) \in \partial \phi(\mathbf{u}^{t+1}) + \nabla f(\mathbf{u}^{t+1}).$$

Thus, we conclude that

$$\|-\gamma^t(\mathbf{u}^{t+1} - \mathbf{v}^t) - \nabla f(\mathbf{v}^t) + \nabla f(\mathbf{u}^{t+1})\| \leq C \|\mathbf{u}^{t+1} - \mathbf{v}^t\| \rightarrow 0,$$

where $C = L + \gamma^t$. Let \mathbf{u}^* becomes any accumulation point of $\{\mathbf{u}^{t+1}\}$, called $\{\mathbf{u}^{t_p+1}\} \rightarrow \mathbf{u}^*$, as $p \rightarrow \infty$. Incorporating the lower semi-continuity of $\phi(\mathbf{u})$ and the supreme principle, we obtain that $\lim_{p \rightarrow \infty} \Psi(\mathbf{u}^{t_p+1}) = \Psi(\mathbf{u}^*)$. Thus, we conclude that $\mathbf{0} \in \partial \Psi(\mathbf{u}^*)$. This completes the proof. \square

Proof for Proposition 2

The following Condition 1 is proposed to provide the foundational bounded constraint for deep modules (i.e., GM and DM) to guarantee the convergence of PDM. We prove that the PCM for PDM optimization can converge to a fixed-point with this condition.

Condition 1. For any input \mathbf{u} , the proposed deep modules GM and DM should satisfy $\|\mathcal{T}_{\mathcal{D}} \circ \mathcal{T}_{\mathcal{G}}(\mathbf{u}^t) - \mathbf{u}^t\| \leq \sqrt{c}/\gamma^t$, where $c > 0$, denoted the step 3 and 4 of Alg. 2 as $\mathcal{T}_{\mathcal{G}}$ and $\mathcal{T}_{\mathcal{D}}$ respectively.

Proof. Based on Condition 1, we can prove the convergence of PCM for PDM optimization. For convenience, we denote $\mathcal{T}_{\mathcal{G}}$, $\mathcal{T}_{\mathcal{D}}$ are the operators of step 3 and 4 in Alg. 2 and $\rho^t = \sqrt{c}/\gamma^t$ firstly. Then, based on Condition 1, following inequality is satisfied

$$\|\mathbf{u}^t - \mathbf{u}_d^{t+1}\| = \|\mathcal{T}_{\mathcal{D}} \circ \mathcal{T}_{\mathcal{G}}(\mathbf{u}^t) - \mathbf{u}^t\| \leq \rho^t.$$

For PDM, the \mathcal{C}_{PDM} is defined as $\arg \min_{\mathbf{u}} f(\mathbf{u}) + \frac{\gamma^t}{2} \|\mathbf{u} - \mathbf{u}_d^{t+1}\|^2$. With the first order optimal condition, we have that $\mathbf{0} \in \nabla f(\mathbf{u}_c^{t+1}) + \gamma^t(\mathbf{u}_c^{t+1} - \mathbf{u}_d^{t+1})$. If optimality checking $\|\nabla f(\mathbf{u}_c^t)\| \leq L$ is satisfied, we can have the following inequality, i.e., $\gamma^t \|\mathbf{u}_c^{t+1} - \mathbf{u}_d^{t+1}\| = \|\nabla f(\mathbf{u}^{t+1})\| \leq L$ which

means $\|\mathbf{u}_c^{t+1} - \mathbf{u}_d^{t+1}\| \leq \frac{L}{\gamma^t}$. With the above inequality, we then have that

$$\begin{aligned} \|\mathbf{u}^{t+1} - \mathbf{u}^t\| &= \|\mathbf{u}_c^{t+1} - \mathbf{u}_d^{t+1} + (\mathbf{u}_d^{t+1} - \mathbf{u}^t)\| \\ &\leq \frac{L}{\gamma^t} + \rho^t. \end{aligned} \quad (13)$$

When $\|\nabla f(\mathbf{u}_d^t)\| \leq L$ is not satisfied, we set $\mathbf{u}^{t+1} \leftarrow \mathbf{u}^t$. Obviously, the above inequality of Eq. (13) is also achieved. As for \mathbf{u}_d^{t+1} , with Condition 1 we have that

$$\begin{aligned} \|\mathbf{u}_d^{t+1} - \mathbf{u}_d^t\| &= \|\mathcal{T}_D \circ \mathcal{T}_G(\mathbf{u}^t) - \mathcal{T}_D \circ \mathcal{T}_G(\mathbf{u}^{t-1})\| \\ &\leq \rho^t + \rho^{t-1} + \frac{L}{\gamma^{t-1}} \end{aligned}$$

Thus, sequence $\{\mathbf{u}^t, \mathbf{u}_d^t\}$ is a Cauchy sequence. This implies that there exists fixed point \mathbf{u}^* satisfying $\mathbf{u}^t \rightarrow \mathbf{u}^*$ as $t \rightarrow \infty$. \square

Proof for Proposition 3

We first consider following Condition 2 to introduce the convergent application scenarios of AN and the proof of Proposition 3 is based on this condition.

Condition 2. *The function f is ρ -strong convex and its gradient is Lipschitz with constant L , where $\rho > 0$ and $L > 0$. ϕ is proper convex function.*

Proof. Based on the above Condition 2, we can prove the fixed-point convergence of AN. In accordance with Condition 2 of the convexity of ϕ , the nonexpansive property of $\text{prox}_{\gamma, \phi}(\mathbf{u}_d^{t+1} - \frac{1}{\gamma^t} \nabla f(\mathbf{u}_d^{t+1}))$ holds [72] which means

$$\begin{aligned} &\|\mathcal{T}_C(\mathbf{u}_d^{t+1}) - \mathcal{T}_C(\mathbf{u}_d^t)\|^2 \\ &\leq \|\mathbf{u}_d^{t+1} - \frac{1}{\gamma^t} \nabla f(\mathbf{u}_d^{t+1}) - \mathbf{u}_d^t + \frac{1}{\gamma^t} \nabla f(\mathbf{u}_d^t)\|^2 \\ &= \|\mathbf{u}_d^{t+1} - \mathbf{u}_d^t\|^2 - \frac{2}{\gamma^t} \langle \nabla f(\mathbf{u}_d^{t+1}) - \nabla f(\mathbf{u}_d^t), \mathbf{u}_d^{t+1} - \mathbf{u}_d^t \rangle \\ &\quad + (\frac{1}{\gamma^t})^2 \|\nabla f(\mathbf{u}_d^{t+1}) - \nabla f(\mathbf{u}_d^t)\|^2, \end{aligned}$$

where we denote \mathcal{T}_G , \mathcal{T}_D and \mathcal{T}_C as the operators of GDC propagation respectively. Since f is ρ -strong convex based on Condition 2, then we have that [73],

$$\begin{aligned} \langle \nabla f(\mathbf{u}_d^{t+1}) - \nabla f(\mathbf{u}_d^t), \mathbf{u}_d^{t+1} - \mathbf{u}_d^t \rangle &\geq \frac{\rho L}{\rho + L} \|\mathbf{u}_d^{t+1} - \mathbf{u}_d^t\|^2 \\ &\quad + \frac{1}{\rho + L} \|\nabla f(\mathbf{u}_d^{t+1}) - \nabla f(\mathbf{u}_d^t)\|^2. \end{aligned}$$

Combining with the above two inequalities, we have

$$\begin{aligned} \|\mathcal{T}_C(\mathbf{u}_d^{t+1}) - \mathcal{T}_C(\mathbf{u}_d^t)\|^2 &\leq (1 - \frac{2\rho L}{\gamma^t(\rho + L)}) \|\mathbf{u}_d^{t+1} - \mathbf{u}_d^t\|^2 \\ &\quad + ((\frac{1}{\gamma^t})^2 - \frac{2}{\gamma^t(\rho + L)}) \|\nabla f(\mathbf{u}_d^{t+1}) - \nabla f(\mathbf{u}_d^t)\|^2. \end{aligned}$$

Therefore, for any $\gamma^t \geq \frac{\rho + L}{2}$, we have $\|\mathcal{T}_C(\mathbf{u}_d^{t+1}) - \mathcal{T}_C(\mathbf{u}_d^t)\| \leq \sqrt{1 - \frac{2\rho L}{\gamma^t(\rho + L)}} \|\mathbf{u}_d^{t+1} - \mathbf{u}_d^t\|$. With the augmentation of AN, assuming that the inner deep classifier of DM has K layers, we have that

$$\|\mathcal{D}(\mathbf{u}_g^{t+1}) - \mathcal{D}(\mathbf{u}_g^t)\| / \|\mathbf{u}_g^{t+1} - \mathbf{u}_g^t\| \leq \prod_{k=1}^K \max_{\mathbf{u}^t \neq \mathbf{0}} \frac{\|\tilde{\omega}_d \mathbf{u}_g^{t+1}\|}{\|\mathbf{u}_g^{t+1}\|} \leq \delta_d,$$

where $\tilde{\omega}_d$ denotes the normalized weights. The above equation implies that

$$\begin{aligned} &\|\mathbf{u}_g^{t+1} + \mathcal{D}(\mathbf{u}_g^{t+1}) - \mathbf{u}_g^{t+1} - (\mathbf{u}_g^t + \mathcal{D}(\mathbf{u}_g^t))\|^2 \\ &\leq \delta_d^2 \|\mathbf{u}_g^{t+1} - \mathbf{u}_g^t\|^2. \end{aligned}$$

The above inequality yields

$$\frac{1}{(1 + \frac{\delta_d}{2})^2} \|\mathcal{T}_D(\mathbf{u}_g^{t+1}) - \mathcal{T}_D(\mathbf{u}_g^t)\|^2 + \frac{1 - \delta_d^2}{(1 + \delta_d)^2} \|\mathbf{u}_g^{t+1} - \mathbf{u}_g^t\|^2 - \frac{1}{1 + \delta_d} \langle \mathbf{u}_g^{t+1} - \mathbf{u}_g^t, \frac{1}{1 + \delta_d} (\mathcal{T}_D(\mathbf{u}_g^{t+1}) - \mathcal{T}_D(\mathbf{u}_g^t)) \rangle \leq 0.$$

According to the properties of averaged nonexpansive operators in [74], we know that $\frac{\mathcal{T}_D(\mathbf{u}_g^{t+1})}{1 + \delta_d}$ is $\frac{\delta_d}{1 + \delta_d}$ -averaged and also is nonexpansive, thus $\mathcal{T}_D(\mathbf{u}_g^{t+1})$ is $(1 + \delta_d)$ -Lipschitz. Similarly, we have $\mathcal{T}_G(\mathbf{u}^t)$ is $(1 + \delta_g)$ -Lipschitz. We denote that $\mathcal{T}(\mathbf{u}^t) = \mathcal{T}_C \circ \mathcal{T}_D \circ \mathcal{T}_G(\mathbf{u}^t)$. Combining the Lipschitz property of $\mathcal{T}_G(\mathbf{u}^t)$, $\mathcal{T}_D(\mathbf{u}_g^{t+1})$ and $\mathcal{T}_C(\mathbf{u}_d^{t+1})$, we conclude that

$$\begin{aligned} \|\mathcal{T}(\mathbf{u}^{t+1}) - \mathcal{T}(\mathbf{u}^t)\| &= \|\mathcal{T}_C \circ \mathcal{T}_D \circ \mathcal{T}_G(\mathbf{u}^{t+1}) - \mathcal{T}_C \circ \mathcal{T}_D \circ \mathcal{T}_G(\mathbf{u}^t)\| \\ &\leq \sqrt{1 - \frac{2\rho L}{\gamma^t(\rho + L)}} \|\mathcal{T}_D \circ \mathcal{T}_G(\mathbf{u}^{t+1}) - \mathcal{T}_D \circ \mathcal{T}_G(\mathbf{u}^t)\| \\ &\leq \sqrt{1 - \frac{2\rho L}{\gamma^t(\rho + L)}} (1 + \delta_d)(1 + \delta_g) \|\mathbf{u}^{t+1} - \mathbf{u}^t\|. \end{aligned}$$

We set $\delta = \sqrt{1 - \frac{2\rho L}{\gamma^t(\rho + L)}} (1 + \delta_d)(1 + \delta_g)$. Then we have that \mathcal{T} is δ -Lipschitz. Obviously, if $\frac{\rho + L}{2} \leq \gamma^t \leq \frac{2\rho L}{\rho + L} (1 + \frac{1}{(1 + \delta_d)^2(1 + \delta_g)^2 - 1})$ constant of $\mathcal{T}(\mathbf{u}^t)$ is less than 1. Indeed, such a γ^t exists if $(1 + \delta_d)(1 + \delta_g) < \frac{\rho + L}{|\rho - L|}$. Then, there exists \mathbf{u}^* satisfying $\mathbf{u}^* = \mathcal{T}(\mathbf{u}^*)$. Obviously, $\|\mathbf{u}^{t+1} - \mathbf{u}^t\| \rightarrow 0$ as $t \rightarrow \infty$ and the sum of $\|\mathbf{u}^{t+1} - \mathbf{u}^t\|$ is bounded, i.e., $\sum_{t=1}^{\infty} \|\mathbf{u}^{t+1} - \mathbf{u}^t\| < \infty$. This means that the propagative sequence converges to a fixed-point. \square

REFERENCES

- [1] H. Zhang, D. Wipf, and Y. Zhang, "Multi-image blind deblurring using a coupled adaptive sparse prior," in *Proc. IEEE Conf. Comput. Vis. Pattern Recognit.*, 2013, pp. 1051–1058.
- [2] S. Roth and M. J. Black, "Fields of experts," *Inter. Jour. Comput. Vis.*, vol. 82, no. 2, p. 205, 2009.
- [3] C. Tomasi and R. Manduchi, "Bilateral filtering for gray and color images," in *Proc. IEEE Conf. Int. Conf. Comput. Vis.*, 1998, pp. 839–846.
- [4] L. Xu, J. S. Ren, C. Liu, and J. Jia, "Deep convolutional neural network for image deconvolution," in *Proc. Advances in Neural Inf. Process. Systems*, 2014, pp. 1790–1798.
- [5] R. Liu, Y. He, S. Cheng, X. Fan, and Z. Luo, "Learning collaborative generation correction modules for blind image deblurring and beyond," *ACM. Inter. Conf. Multi.Media*, pp. 1921–1929, 2018.
- [6] D. Sun, X. Yang, M.-Y. Liu, and J. Kautz, "PWC-Net: CNNs for optical flow using pyramid, warping, and cost volume," in *Proc. IEEE Conf. Comput. Vis. Pattern Recognit.*, 2018, pp. 8934–8943.
- [7] E. Ilg, N. Mayer, T. Saikia, M. Keuper, A. Dosovitskiy, and T. Brox, "FlowNet 2.0: Evolution of optical flow estimation with deep networks," in *Proc. IEEE Conf. Comput. Vis. Pattern Recognit.*, 2017, pp. 1647–1655.
- [8] T.-W. Hui, X. Tang, and C. C. Loy, "LiteflowNet: A lightweight convolutional neural network for optical flow estimation," in *Proc. IEEE Conf. Comput. Vis. Pattern Recognit.*, 2018.
- [9] A. Geiger, P. Lenz, and R. Urtasun, "Are we ready for autonomous driving? the kitti vision benchmark suite," in *Proc. IEEE Conf. Comput. Vis. Pattern Recognit.*, 2012.
- [10] R. Liu, Y. Zhang, S. Cheng, X. Fan, and Z. Luo, "A theoretically guaranteed deep optimization framework for robust compressive sensing mri," in *AAAI*, vol. 33, 2019, pp. 4368–4375.
- [11] G. Balakrishnan, A. Zhao, M. R. Sabuncu, J. Guttag, and A. V. Dalca, "Voxelmorph: a learning framework for deformable medical image registration," *IEEE transactions on medical imaging*, pp. 1788–1800, 2019.
- [12] R. Liu, G. Zhong, J. Cao, Z. Lin, S. Shan, and Z. Luo, "Learning to diffuse: A new perspective to design pdes for visual analysis," *IEEE Trans. Pattern Anal. Mach. Intell.*, pp. 2457–2471, 2016.
- [13] R. Liu, Z. Lin, W. Zhang, and Z. Su, "Learning pdes for image restoration via optimal control," in *Proc. Eur. Conf. Comput. Vis.*, 09 2010, pp. 115–128.
- [14] D. Perrone and P. Favaro, "Total variation blind deconvolution: The devil is in the details," in *Proc. IEEE Conf. Comput. Vis. Pattern Recognit.*, 2014, pp. 2909–2916.
- [15] S. Nah, T. H. Kim, and K. M. Lee, "Deep multi-scale convolutional neural network for dynamic scene deblurring," in *Proc. IEEE Conf. Comput. Vis. Pattern Recognit.*, 2017.

- [16] H. Wang, Q. Xie, Q. Zhao, and D. Meng, "A model-driven deep neural network for single image rain removal," in *Proc. IEEE Conf. Comput. Vis. Pattern Recognit.*, June 2020.
- [17] W. Dong, P. Wang, W. Yin, G. Shi, F. Wu, and X. Lu, "Denoising prior driven deep neural network for image restoration," *IEEE Trans. Pattern Anal. Mach. Intell.*, pp. 2305–2318, 2019.
- [18] R. Aljadaany, D. K. Pal, and M. Savvides, "Douglas-rachford networks: Learning both the image prior and data fidelity terms for blind image deconvolution," in *Proc. IEEE Conf. Comput. Vis. Pattern Recognit.*, June 2019.
- [19] S. Zheng, S. Jayasumana, B. Romera-Paredes, V. Vineet, Z. Su, D. Du, C. Huang, and P. H. Torr, "Conditional random fields as recurrent neural networks," in *Proc. IEEE Conf. Comput. Vis. Pattern Recognit.*, 2015, pp. 1529–1537.
- [20] J. Pan, Z. Hu, Z. Su, and M.-H. Yang, "Deblurring text images via l0-regularized intensity and gradient prior," in *Proc. IEEE Conf. Comput. Vis. Pattern Recognit.*, 2014, pp. 2901–2908.
- [21] D. Krishnan and R. Fergus, "Fast image deconvolution using hyper-laplacian priors," in *Proc. Advances in Neural Inf. Process. Systems*, 2009, pp. 1033–1041.
- [22] J. Pan, D. Sun, H. Pfister, and M. H. Yang, "Deblurring images via dark channel prior," in *IEEE Trans. Pattern Anal. Mach. Intell.*, vol. 40, no. 99, 2018, pp. 2315–2328.
- [23] Y. Yan, W. Ren, Y. Guo, R. Wang, and X. Cao, "Image deblurring via extreme channels prior," in *Proc. IEEE Conf. Comput. Vis. Pattern Recognit.*, 2017, pp. 4003–4011.
- [24] G. B. Passty, "Ergodic convergence to a zero of the sum of monotone operators in hilbert space," in *Journal of Mathematical Analysis and Applications*, 1979, pp. 383–390.
- [25] A. Beck and M. Teboulle, "A fast iterative shrinkage-thresholding algorithm for linear inverse problems," *SIAM Journal on Imaging Sciences*, vol. 2, no. 1, pp. 183–202, 2009.
- [26] Z. Lin, R. Liu, and H. Li, "Linearized alternating direction method with parallel splitting and adaptive penalty for separable convex programs in machine learning," in *Machine Learning*, 2015.
- [27] X. Liu, M. Suganuma, Z. Sun, and T. Okatani, "Dual residual networks leveraging the potential of paired operations for image restoration," in *Proc. IEEE Conf. Comput. Vis. Pattern Recognit.*, 2019.
- [28] C. Ledig, L. Theis, F. Huszar, J. Caballero, A. Cunningham, A. Acosta, A. P. Aitken, A. Tejani, J. Totz, Z. Wang, and W. Shi, "Photo-realistic single image super-resolution using a generative adversarial network," in *Proc. IEEE Conf. Comput. Vis. Pattern Recognit.*, 2017, pp. 105–114.
- [29] S. Li, B. Qin, J. Xiao, Q. Liu, Y. Wang, and D. Liang, "Multi-channel and multi-model-based autoencoding prior for grayscale image restoration," *IEEE Trans. Image Process.*, vol. 29, pp. 142–156, 2019.
- [30] U. Schmidt and S. Roth, "Shrinkage fields for effective image restoration," in *Proc. IEEE Conf. Comput. Vis. Pattern Recognit.*, June 2014, pp. 2774–2781.
- [31] L. Xiao, J. Wang, W. Heidrich, and M. Hirsch, "Learning high-order filters for efficient blind deconvolution of document photographs," in *Proc. Eur. Conf. Comput. Vis.*, 2016, pp. 734–749.
- [32] K. Zhang, W. Zuo, S. Gu, and L. Zhang, "Learning deep cnn denoiser prior for image restoration," in *Proc. IEEE Conf. Comput. Vis. Pattern Recognit.*, 2017.
- [33] K. Zhang, W. Zuo, and L. Zhang, "Deep plug-and-play super-resolution for arbitrary blur kernels," in *Proc. IEEE Conf. Comput. Vis. Pattern Recognit.*, 2019, pp. 1671–1681.
- [34] E. K. Ryu, J. Liu, S. Wang, X. Chen, Z. Wang, and W. Yin, "Plug-and-play methods provably converge with properly trained denoisers," *arXiv preprint arXiv:1905.05406*, 2019.
- [35] L. Xu, C. Lu, Y. Xu, and J. Jia, "Image smoothing via l0 gradient minimization," *ACM TOG*, vol. 30, no. 6, p. 174, 2011.
- [36] L. Sun, S. Cho, J. Wang, and J. Hays, "Edge-based blur kernel estimation using patch priors," in *Proc. IEEE Int. Conf. Comput. Photography*, 2013, pp. 1–8.
- [37] W. Ren, J. Zhang, L. Ma, J. Pan, X. Cao, W. Zuo, W. Liu, and M.-H. Yang, "Deep non-blind deconvolution via generalized low-rank approximation," in *Proc. Advances in Neural Inf. Process. Systems*, 2018, pp. 297–307.
- [38] W. Yang, R. T. Tan, J. Feng, J. Liu, Z. Guo, and S. Yan, "Deep joint rain detection and removal from a single image," in *Proc. IEEE Conf. Comput. Vis. Pattern Recognit.*, 2017.
- [39] X. Li, J. Wu, Z. Lin, H. Liu, and H. Zha, "Recurrent squeeze-and-excitation context aggregation net for single image deraining," in *ECCV*, 2018, pp. 254–269.
- [40] G. Li, X. He, W. Zhang, H. Chang, L. Dong, and L. Lin, "Non-locally enhanced encoder-decoder network for single image deraining," in *ACM Inter. Conference on Multimedia*, 2018, pp. 1056–1064.
- [41] D. Ren, W. Zuo, Q. Hu, P. Zhu, and D. Meng, "Progressive image deraining networks: A better and simpler baseline," in *Proc. IEEE Conf. Comput. Vis. Pattern Recognit.*, 2019, pp. 3937–3946.
- [42] H. Zhang, Y. Li, H. Chen, and C. Shen, "Memory-efficient hierarchical neural architecture search for image denoising," in *Proc. IEEE Conf. Comput. Vis. Pattern Recognit.*, 2020, pp. 3657–3666.
- [43] H. Liu, K. Simonyan, and Y. Yang, "Darts: Differentiable architecture search," *arXiv preprint arXiv:1806.09055*, 2018.
- [44] J. He, C. Dong, and Y. Qiao, "Modulating image restoration with continual levels via adaptive feature modification layers," in *Proc. IEEE Conf. Comput. Vis. Pattern Recognit.*, June 2019.
- [45] Y. Chen, W. Yu, and T. Pock, "On learning optimized reaction diffusion processes for effective image restoration," in *Proc. IEEE Conf. Comput. Vis. Pattern Recognit.*, 2015, pp. 5261–5269.
- [46] Y. Yang, J. Sun, H. Li, and Z. Xu, "Deep admn-net for compressive sensing mri," in *Proc. Advances in Neural Inf. Process. Systems*. Curran Associates, Inc., 2016, pp. 10–18.
- [47] S. H. Chan, X. Wang, and O. A. Elgendy, "Plug-and-play admn for image restoration: Fixed-point convergence and applications," *IEEE Trans. Comput. Imaging*, vol. 3, no. 1, pp. 84–98, 2017.
- [48] R. Liu, X. Fan, M. Hou, Z. Jiang, and Z. Luo, "Learning aggregated transmission propagation network for haze removal and beyond," *IEEE Trans. Neural Net. Learning sys.*, 2018.
- [49] D. Martin, C. Fowlkes, D. Tal, and J. Malik, "A database of human segmented natural images and its application to evaluating segmentation algorithms and measuring ecological statistics," in *Proc. IEEE Conf. Comput. Vis. Pattern Recognit.*, vol. 2. IEEE, 2001, pp. 416–423.
- [50] T. Miyato, T. Kataoka, M. Koyama, and Y. Yoshida, "Spectral normalization for generative adversarial networks," in *International Conference on Learning Representations*, February 2018.
- [51] Y. Yoshida and T. Miyato, "Spectral norm regularization for improving the generalizability of deep learning," *arXiv preprint arXiv:1705.10941*, 2017.
- [52] S. Woo, J. Park, J.-Y. Lee, and I. So Kweon, "Cbam: Convolutional block attention module," in *Proc. Eur. Conf. Comput. Vis.*, 2018, pp. 3–19.
- [53] J. Hu, L. Shen, and G. Sun, "Squeeze-and-excitation networks," in *Proc. IEEE Conf. Comput. Vis. Pattern Recognit.*, 2018, pp. 7132–7141.
- [54] C. Zach, T. Pock, and H. Bischof, "A duality based approach for realtime tv-l1 optical flow," in *Joint pattern recognition symposium*, 2007, pp. 214–223.
- [55] W. Zuo, D. Meng, L. Zhang, and X. Feng, "A generalized iterated shrinkage algorithm for non-convex sparse coding," in *Proc. IEEE Conf. Int. Conf. Comput. Vis.*, 2013, pp. 217–224.
- [56] L. Xu and J. Jia, "Two-phase kernel estimation for robust motion deblurring," in *Proc. Eur. Conf. Comput. Vis.*, 2010, pp. 157–170.
- [57] A. Levin, Y. Weiss, F. Durand, and W. T. Freeman, "Understanding and evaluating blind deconvolution algorithms," in *Proc. IEEE Conf. Comput. Vis. Pattern Recognit.*, 2009, pp. 1964–1971.
- [58] J. Kruse, C. Rother, and U. Schmidt, "Learning to push the limits of efficient fft-based image deconvolution," in *Proc. IEEE Conf. Comput. Vis. Pattern Recognit.*, 2017, pp. 4586–4594.
- [59] D. J. Butler, J. Wulff, G. B. Stanley, and M. J. Black, "A naturalistic open source movie for optical flow evaluation," in *Proc. Eur. Conf. Comput. Vis.*, Oct. 2012, pp. 611–625.
- [60] D. Zoran and Y. Weiss, "From learning models of natural image patches to whole image restoration," in *Proc. IEEE Conf. Int. Conf. Comput. Vis.*, 2011, pp. 479–486.
- [61] N. Yair and T. Michaeli, "Multi-scale weighted nuclear norm image restoration," in *Proc. IEEE Conf. Comput. Vis. Pattern Recognit.*, 2018.
- [62] C. Li, W. Yin, H. Jiang, and Y. Zhang, "An efficient augmented lagrangian method with applications to total variation minimization," *Computational Optimization and Applications*, vol. 56, no. 3, pp. 507–530, 2013.
- [63] A. Dosovitskiy, P. Fischer, E. Ilg, V. Golkov, and T. Brox, "Flownet: Learning optical flow with convolutional networks," in *Proc. IEEE Conf. Int. Conf. Comput. Vis.*, Dec 2015.
- [64] A. Ranjan and M. J. Black, "Optical flow estimation using a spatial pyramid network," in *Proc. IEEE Conf. Comput. Vis. Pattern Recognit.*, 2017.

- [65] D. Krishnan, T. Tay, and R. Fergus, "Blind deconvolution using a normalized sparsity measure," in *Proc. IEEE Conf. Comput. Vis. Pattern Recognit.*, 2011, pp. 233–240.
- [66] A. Levin, Y. Weiss, F. Durand, and W. T. Freeman, "Efficient marginal likelihood optimization in blind deconvolution," in *Proc. IEEE Conf. Comput. Vis. Pattern Recognit.*, 2011, pp. 2657–2664.
- [67] L. Li, J. Pan, W. S. Lai, C. Gao, and M. H. Yang, "Learning a discriminative prior for blind image deblurring," *Proc. IEEE Conf. Comput. Vis. Pattern Recognit.*, pp. 6616–6625, 2018.
- [68] L. He and Y. Wang, "Iterative support detection-based split bregman method for wavelet frame-based image inpainting," *IEEE Trans. Image Process.*, vol. 23, no. 12, pp. 5470–5485, 2014.
- [69] P. Getreuer, "Total variation inpainting using split bregman," *Image Processing On Line*, vol. 2, pp. 147–157, 2012.
- [70] Z. Farbman, R. Fattal, D. Lischinski, and R. Szeliski, "Edge-preserving decompositions for multi-scale tone and detail manipulation," *ACM TOG*, vol. 27, no. 3, p. 67, 2008.
- [71] L. Xu, Q. Yan, Y. Xia, and J. Jia, "Structure extraction from texture via natural variation measure," *ACM TOG*, 2012.
- [72] H. H. Bauschke, P. L. Combettes *et al.*, *Convex analysis and monotone operator theory in Hilbert spaces*. Springer, 2011, vol. 408.
- [73] N. Yu, "Introductory lectures on convex optimization: a basic course," 2004.
- [74] H. Bauschke and P. Combettes, *Convex Analysis and Monotone Operator Theory in Hilbert Spaces*, January 2017.